# Optimising stellarator magnetic geometry for increased critical gradient of trapped-electron modes

Chennakeshava, Nishith

*Award date:*
2019

# Optimising Stellarator Magnetic Geometry for Increased Critical Gradient of Trapped-Electron Modes

Nishith Chennakeshava

Under the Supervision of
Dr. J.H.E. Proll
and
Dr. H.E. Mynick

**Abstract**

Stellarators have historically suffered from high levels of neoclassical transport, which has limited their ability to confine energy. However, with the introduction of optimised stellarators such as W7-X, HSX, etc., neoclassical transport is not the main limiting factor anymore. The current expectation is that turbulence will be the dominant transport channel. It also sets the energy confinement time in a reactor. Therefore, it is crucial that stellarators are optimised for a lower level of turbulent transport. Stellarators have approximately 10 times more degrees of freedom in shaping the magnetic surfaces, when compared to a tokamak. This gives us the opportunity to change properties of the magnetic field of the stellarator, to reduce the level of turbulent transport.

Turbulence is driven by gradients in both density and temperature. This work aims to shift the density gradient at which turbulence starts to grow i.e., the critical gradient, to a higher value of the density gradient. This thesis focuses on the Trapped Electron Mode (TEM) turbulent transport channel driven by density gradients. A specialised code could be used to carry out the optimisation process, which reshapes the magnetic surfaces to have higher critical gradients. This will allow stellarators to operate at higher density gradients without TEM turbulence playing a significant limiting role. A gyrokinetic code can be used as the cost function in such a code. However, it is computationally prohibitive to use gyrokinetic codes to calculate the critical gradients within an optimisation loop. Therefore, a dispersion relation of the TEM at the critical gradient is used to relate the critical gradient and the magnetic geometry. This relation is then used as a proxy, for the optimisation process. Then, the resulting magnetic configuration with a shifted TEM critical gradient can be validated using linear runs of a gyrokinetic code.

The derived proxy was then calculated for multiple devices, and compared to gyrokinetic simulations. However, it yielded a weak negative correlation. This is most likely due to the choice of frequency orderings that were made to obtain the proxy. An alternative pathway to obtain a proxy has been proposed, which does not rely on making the same frequency ordering choices.

# Contents

**1 Introduction** **1**
1.1 Motivation . . . 3
1.2 Research Question . . . 5

**2 Gyrokinetics** **7**
2.1 Microinstabilities . . . 8
2.2 An Outline of the Gyrokinetic Equation . . . 9
2.3 Quasi-neutrality . . . 15

**3 Derivation of the Dispersion Relation** **17**
3.1 Outline of Assumptions . . . 17
3.2 The Dispersion Relation . . . 17

**4 Derivation of the Proxy** **20**

**5 Results** **24**

**6 Discussion** **37**

**7 An Alternative Approach** **38**

**8 Conclusion** **41**

**A The Numerical Calculation of the Proxy** **45**

**B Discrepancies in the Numerical Solutions** **48**

# 1 Introduction

The demand for energy is ever growing, as more people around the world experience a liberation from poverty. Energy consumption is an indicator of quality of life. As such, it is very important that we continue to meet the ever increasing energy demands of the world as more countries aim to lift their standards of living, and consume more energy along the way. However, this creates a unique problem for policy makers in light of global warming. Although increasing fossil fuel based plants is an option, it is not a good one as it contributes quite heavily to global warming. So it is crucial that we supply the said increase in energy, in the cleanest, and carbon free/neutral way possible. Renewable energy technologies like solar or wind have come a long way since their introduction, but they still suffer from intermittency and unreliable energy production. The key is energy density, which determines the amount of energy a source can produce given an area of land. Although solar and other renewable technology are excellent sources, they suffer from being a low energy density source of energy (Layton, 2008). Nuclear fission reactors on the other hand, offers very high energy density, but is generally held in low esteem by the general public.

Therefore, we need a source that has high energy density, is carbon free/neutral, is safe, and does not have a negative connotation attached to it. This is where fusion enters the fray. Although the public's perception of fusion is ever so slightly tainted due to its "nuclear" nature, it does not suffer from it as badly as nuclear fission. Thus it satisfies all the requirements that we are looking for in an energy source except for one, which is that it does not exist in a commercial capacity as of yet. However, considering the unforgiving deadline that we have set upon ourselves due to global warming, the world has come together to fund research into fusion, and make it a commercial reality as soon as possible. The 'Fusion Roadmap' compiled by the European Fusion Development Agreement (EFDA) cites 2050 as the possible target for commercially available fusion reactors (Romanelli et al., 2013).

In 1957, Lawson showed that magnetically confined fusion plasmas can indeed give net energy, if it meets the triple product, $n_i T_i \tau_E > 4 \times 10^{21} keV m^{-3} s$, ($n_i$ is the ion density, $T_i$ is the ion temperature, and $\tau_E$ is the energy confinement time) for a Deuterium-Tritium based plasma (Lawson, 1957). Tokamaks showed great promise when it came to confinement properties, but a second method to achieve magnetic confinement fusion, the stellarator was not far behind. Currently, stellarators are widely considered to be a generation behind the tokamak.

Although tokamaks and stellarators both use helical magnetic fields to confine the plasma, the magnetic geometry of the two concepts is fundamentally different. In a tokamak, the magnetic field strength is constant in the toroidal direction giving us an axisymmetric device. Stellarators lack this toroidal symmetry. While both types of reactors have magnetic minima where particles can be trapped, the tokamak has only one such region while the stellarator could have multiple regions that act as magnetic mirrors. But seeing as tokamkas require a current in the plasma to produce the helical field, stellarators have many features that are advantageous, compared to tokamaks such as disruption free performance, and the absence of a current drive. Although the fusion roadmap (Romanelli et al., 2013) mainly deals with tokamaks, and the time-line relevant to the development of tokamaks as fusion power plants. However, they do also include stellarators and predict that the first burning plasma stellarator will begin operations, or at least be built in the 2040s.

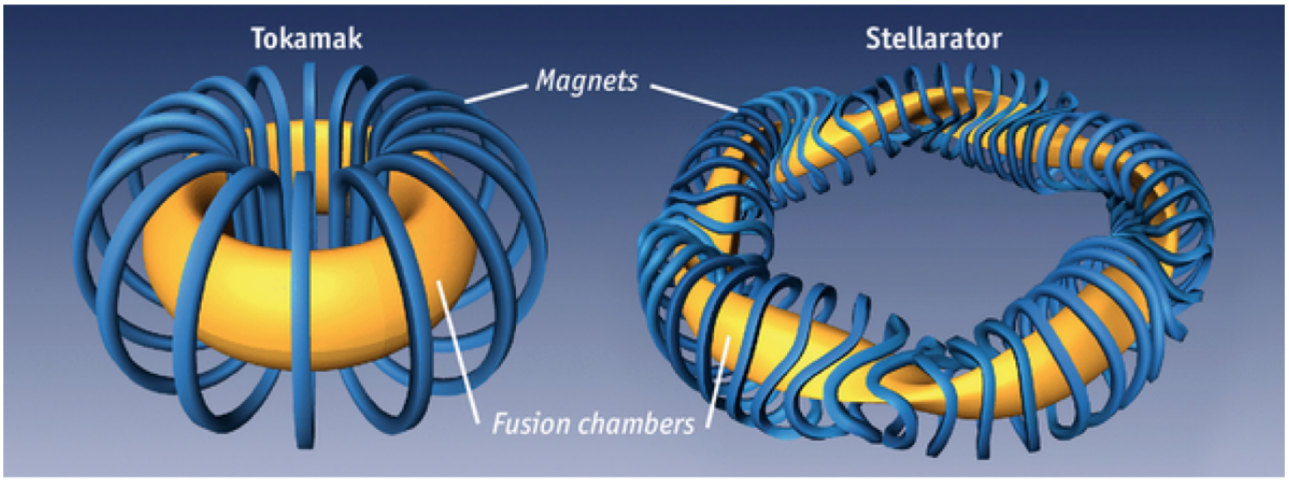


Figure 1: A comparison between a typical tokamak geometry, and the geometry of Wendelstein 7-X. (The Economist, 2015)

There are many combinations of isotopes we can use to achieve fusion. By far the easiest way to achieve fusion is to use deuterium and tritium heated to temperatures of around 15 keV,

$$ {}^{2}_{1}D + {}^{3}_{1}T \rightarrow {}^{4}_{2}He + {}^{1}_{0}n + 17.6MeV. \tag{1.1} $$

But there are many challenges we face in achieving that goal. One of those challenges is to do with turbulent heat and particle transport, which sets the energy confinement time in a reactor and is driven by pressure and density gradients. Therefore it is critical that we have the ability to predict turbulent transport levels in a reactor. Turbulence causes the transport of particles, momentum, and energy. This is believed to originate from plasma microinstabilities (chapter 2.1). It is important to note that even if the plasma is stable to MHD instabilities, drift waves can be destabilised by high density and temperature gradients (Tang, 1978; Horton, 1999). This is characterised by what is known as the critical gradient (threshold). It is a point in the normalised density (or temperature gradient) beyond which these instabilities grow, which is defined as

$$ \frac{R}{L_n} = -\frac{R}{n_a}\nabla n_a, \tag{1.2} $$

where R is the major radius of the magnetic confinement device, and $n_a$ is the density of the particle species 'a'. Stellarator turbulence growth rates display a different behaviour to that of tokamaks (figure 2). We notice that while tokamaks have a higher critical gradient, while also having a higher growth rate. Conversely stellarators have a lower threshold, but also a lower growth rate.

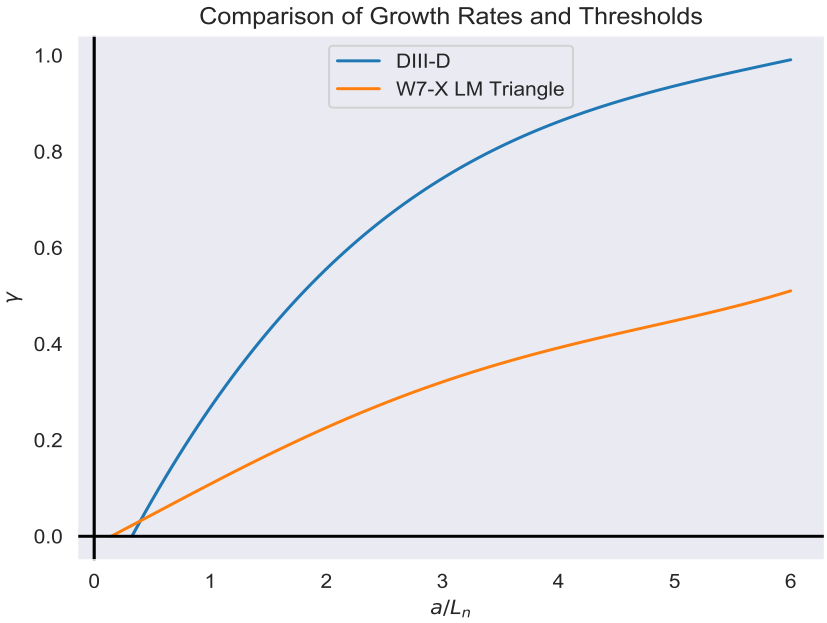


Figure 2: The graph displays the comparison of growth rates between tokamaks (DIII-D) and stellarators (W7-X, low mirror configuration, triangle flux tube). While tokamaks have a higher threshold, they also display a higher growth rate. The inverse is true of the stellarators. Here, the 'a' in $a/L_n$ is the minor radius of the reactor.

## 1.1 Motivation

Historically, stellarators have been plagued with bad confinement properties. But the advent of optimised stellarators have shown that neo-classical (NC) transport can be suppressed, and improved upon (Mynick, 2006). Due to its strong temperature dependence (Helander and Sigmar, 2005), neoclassical transport is expected to still be predominant in the high temperature plasma core, but as the temperature decreases strongly towards the plasma edge, neoclassical transport is reduced and turbulent transport becomes important. However, this means that turbulent transport in stellarators is now expected to be the significant channel of transport that has to be suppressed. As confinement time is limited by the energy transport we must possess the ability to manipulate and suppress turbulent transport in stellarators if we are to consider stellarators as a viable competitor for a fusion power plant.

In stellarator plasmas, two turbulent channels which are thought to be responsible for anomalous transport are the ITG (Ion Temperature Gradient) mode, and the TEM (Trapped Electron Mode) (Warmer et al., 2017). Figure (3) shows these regimes, and where they are unstable. We notice that for lower density and temperature gradients, the system is stable to turbulent transport. But once we hit the threshold in either temperature gradients or density gradients, turbulence starts to play a role. The TEMs that we are investigating here are mainly driven unstable by high density gradients as shown in figure (3). Although, when simulated using non-linear simulations, the threshold is more of a 'knee' (Dimits shift) in the temperature gradient driven channels, like the ITG (Dimits et al., 2000). However, others have also noticed an analogous effect in the density gradient driven TEMs (Ernst et al., 2009). But this effect is not relevant to this thesis, as this thesis only deals with linear simulations.

In the outer third of the minor radius, it is shown that the turbulent losses overcome NC transport in Wendelstein 7-AS (W7-AS), even in plasmas with optimum confinement (Hirsch et al., 2008). The outer regions of the plasma also showcase high density gradients, driving a high level of TEM turblence. Therefore, the main mode that we will focus on is the Trapped Electron Mode.

If the temperature gradients are small compared to the density gradients, while ignoring collisions, there are stellarator designs (quasi-isodynamic) that are automatically immune to the ordinary TEM

and to all lower frequency electrostatic instabilities (Proll et al., 2012).

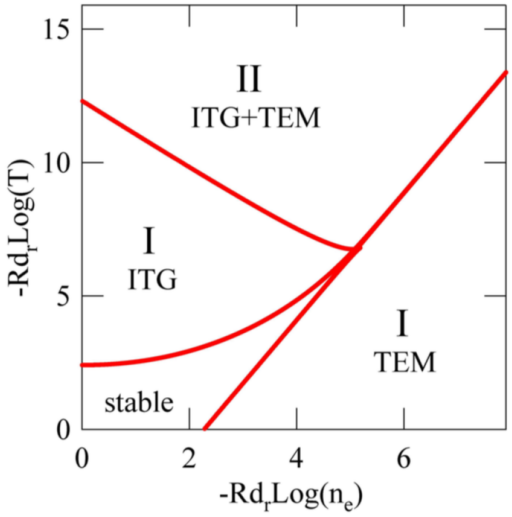


Figure 3: The figure describes the regions of stability/instability as a function of the logarithmic temperature and density gradients (Garbet et al., 2004).

There are two possible ways in which we could approach this problem. The first would be to lower the slope of the growth rate of the TEM past the critical gradient as done in (Proll et al., 2015). The alternative to this approach would be to move the critical gradient to higher density gradients such that the TEM turbulent transport is not a significant factor in a larger part of the stellarator's operational parameter space. In stellarators this can potentially be achieved by manipulating the magnetic surfaces to influence the critical gradient. This is possible as the magnetic surfaces of stellarators can be configured in more ways than a tokamak. Tokamaks have roughly 10 times the number of degrees of freedom (Boozer, 2005) with which it's magnetic field may be manipulated, when compared to a stellarator. The following work compliments the work carried out by Proll et al. (2015), where they have demonstrated a lower slope for the instability growth rate in HSX (Helically Symmetric Experiment).

Therefore, it is desirable to have simplified expressions that can approximate these non-linear fluxes to a great deal of accuracy. Such that we may then use these simplified expressions in optimisation studies of the trapped electron mode.

## 1.2 Research Question

***Is it possible to optimise stellarators to have increased critical gradients for the Trapped-Electron Mode?***

This can be achieved by answering the following questions:

1. Is it possible to derive a relation for the critical gradient of the TEM instability, from a dispersion relation?
2. Can this relation then be implemented in STELLOPT (Reiman et al., 1999), to obtain an optimised configuration?
3. Can the resulting geometry be validated for a higher critical gradient using a gyrokinetic code?

The general procedure to achieve this is to implement a gyrokinetic into an optimiser algorithm (STELLOPT) to achieve the desired magnetic geometry. However, this is infeasible as it is computationally prohibitive. Therefore, the alternative route is chosen where a proxy is used instead of the gyrokinetic code in the optimisation process. The proxy is a simplified expression designed to be included in an optimisation loop that will give an estimate of the critical gradient based on the magnetic geometry of the stellarator. The aim of the proxy function is to provide a means of estimating the stability of a configuration towards TEMs efficiently (Proll et al., 2015). TEMs are explained further in chapter 2.

We can obtain such a proxy by deriving a dispersion relation for the TEM. The critical gradient is then extracted from this dispersion relation. We expect this to depend on quantities of the magnetic field (like the curvature, trapped particle fraction, etc.), and quantities of the plasma like density gradient.

$$C_g = f(\lambda, \kappa, B_{min}, B_{max}, \omega_{drift}, ...) \tag{1.3}$$

where $C_g$ is the critical gradient, $\lambda$ is the pitch angle, $\kappa$ is the curvature, and $\omega_{drift}$ is the drift frequency. Effectively giving us a relation for the threshold as a function of the geometry parameters of the stellarator,

$$thershold = f(geometry) \tag{1.4}$$

Such a proxy function is of course just an estimate of the actual critical gradient. Therefore, an estimate of its accuracy is required before such a proxy is implemented with any optimisation algorithm, testing it with multiple stellarator geometries. A good correlation here would see the proxy implemented in STELLOPT, whose results can then be validated using linear runs of a gyrokinetic code.

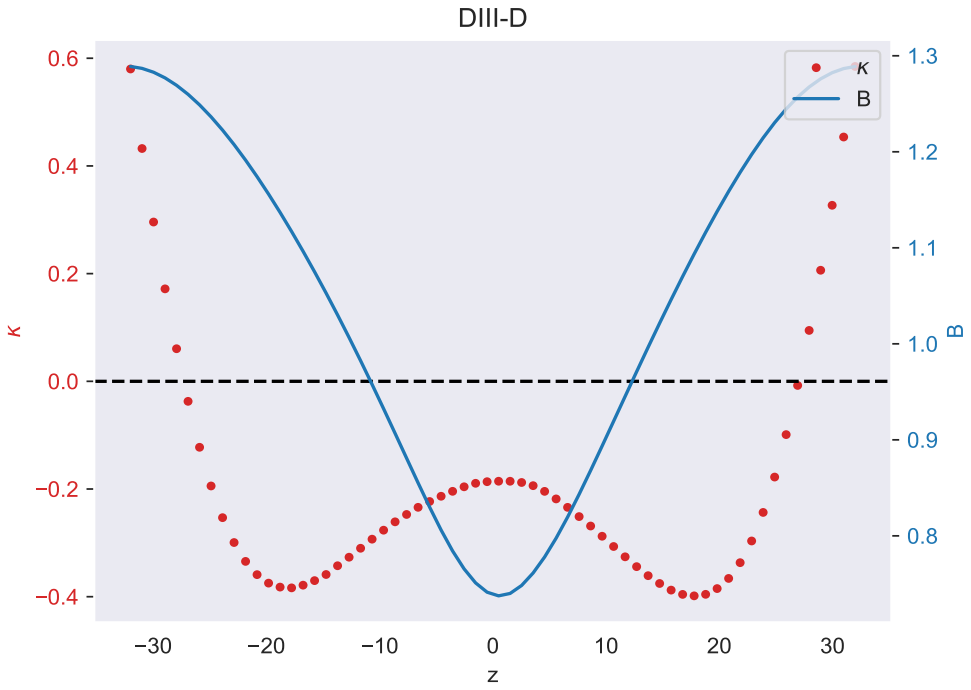


Figure 4: The graph shows the curvature on the left axis, and the magnetic field strength on the right axis for DIII-D (General Atomics, 2018). The data for this graph has been acquired from GIST (Geometry Interface for Stellarators and Tokamaks) output files (Xanthopoulos et al., 2009).

TEMs could be stabilised in multiple ways. Of course the most obvious way to stabilise TEMs is with lower density gradients, and a lower electron temperature gradient, but this is not always an option. Romanelli et al. (2007) describe how TEMs could be stabilised, via collisions, as it effectively decreases the total number of trapped particles due to a de-trapping effect. However, the following work deals with the collisionless regime only. The local shear was put forth as possibly a very important factor in Mynick et al. (2011). Figure (4) hints at a further way in which TEMs could be stabilised in instances where the magnetic field, and the local curvature are out of phase. Proll et al. (2015) explains how many of the trapped particles will have an average bad curvature, if the they are mainly trapped in regions of local bad curvature. Therefore, we expect configurations that have the magnetic field and the curvatures out of phase to have lower TEM growth rates, which does not necessarily result in a higher critical gradient.

Further chapters of this work delve into microinstabilities, and an outline of the derivation of the gyrokinetic equation (chapter 2). After which, the dispersion relation (chapter 3) and the proxy function (chapter 4) is derived. It then goes through the results (chapter 5) obtained, and a brief discussion (chapter 6) of the results. The work concludes by providing an outlook (chapter 7), and a conclusion (chapter 8).

## 2 Gyrokinetics

As we have discussed in the past, turbulent transport is a very important branch of fusion energy to spend time and effort on, as the confinement time ($\tau_E$) is set by level of energy transport, this can be expressed as

$$\tau_E \sim \frac{\tau_c L^2}{\Delta^2}, \tag{2.1}$$

where $\tau_E$ is the energy confinement time, $\Delta$ is the typical cross field eddy size, $\tau_c$ is the turbulent correlation time, and L is the size of the plasma (Cowley, 2018).

We can improve confinement times by breaking up the size of the cross field eddy, such that the random walk of heat and particles across the field is lowered to an acceptable level. This can be achieved via shear flows like zonal flows shown in figure (5), that break up the size of the cross field eddies, and are shown to have a stabilising effect (Biglari et al., 1990; Hahm and Burrell, 1995; Terry, 2000).

Regardless of which, we do require a way to predict turbulent transport. A major branch of transport theory is dedicated to the numerical analysis of turbulent fluxes, and the underlying physics. High temperature plasmas contain a large variety of fluctuations across different spatio-temporal scales (Figure 6). While gyro motion evolves on the scale of ∼GHz, the macroscopic phenomenon tend to evolve at the ∼Hz scales. This makes it highly infeasible to calculate the full system of equations, as it is computationally taxing. The time and spatial scales involved allow us to use gyrokinetics, a kinetic treatment of the plasma.

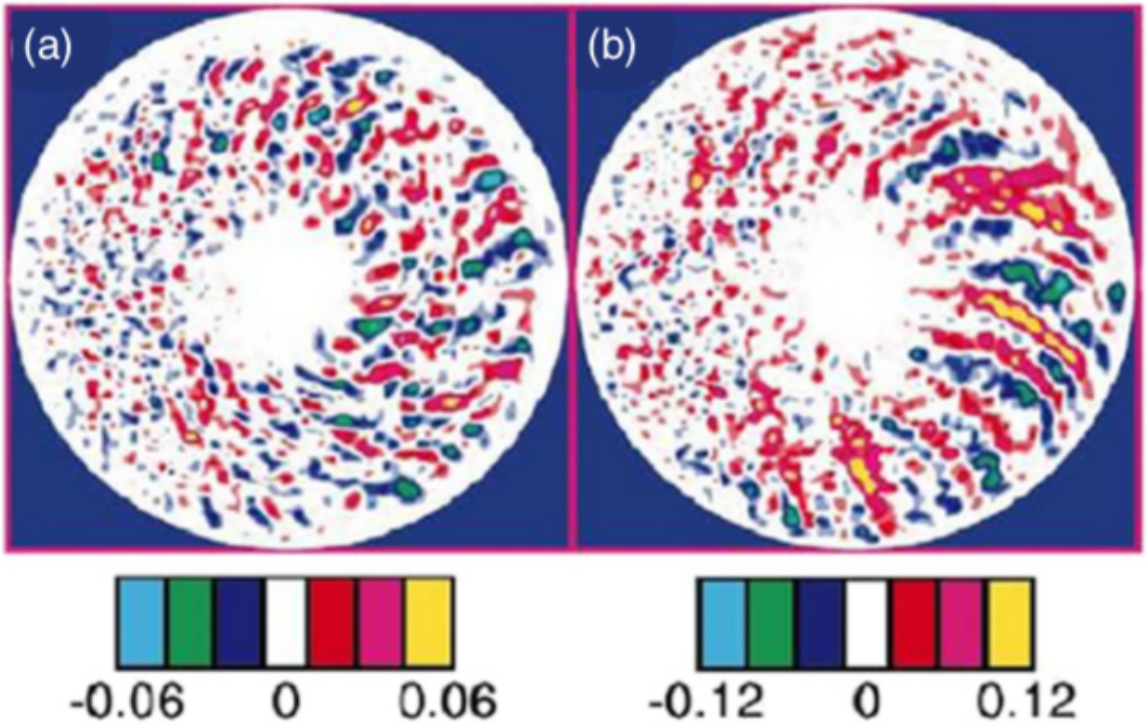


Figure 5: The images show the potential fluctuations in a poloidal cross section of a tokamak as found in the steady state of nonlinear global gyrokinetic simulations. The figure on the left has zonal flows which breaks up the size of the cross field eddies. To highlight differences in the turbulent eddy size, the zonal flow component is filtered out in the plots.(Lin et al., 1998)

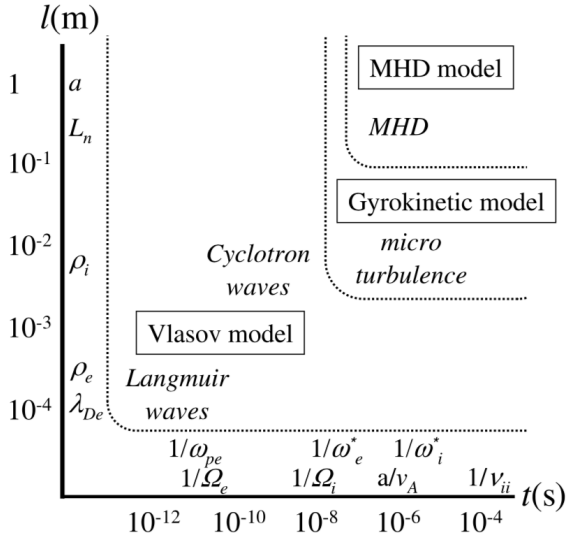


Figure 6: The figure on the left describes the phenomenon present in a fusion plasma as a function of the spacial and temporal scales (Garbet et al., 2010).

In the coming chapter, we will first start with an explanation of microinstabilities that drive the turbulence considered here, move on to outlining the derivation of the gyrokinetic derivation, and close the system of equations with the quasi-neutrality condition.

## 2.1 Microinstabilities

High temperature plasmas contain a large variety of fluctuations across different spatio-temporal scales. This turbulent behaviour causes the transport of particles, momentum, and energy. This originates from plasma microinstabilities. It is important to note that even if the plasma is stable to MHD instabilities, drift waves can be destabilised by high density and temperature gradients (Tang, 1978; Horton, 1999). Microinstabilities mainly draw their energy from gradients in temperature and density. At the point of marginal stability, they are driven by one particle species, and are stabilised by the other.

In fusion core plasmas, there are two types of instability modes that are responsible for turbulent transport, the curvature and slab instabilities. Both these modes arise in the presence of particle drift perpendicular to the particle's motion along the field line, and only the passing particle are affected by the slab mode instability as the development of the slab type instability is independent of the toroidal plasma geometry.

As opposed to the slab type instability, the curvature type instability develops in the presence of an inhomogeneous magnetic field ($\nabla \mathbf{B}$). This introduces a dependency between the diamagnetic drift frequency, curvature, and the magnetic drift frequency. The instability condition for curvature type instabilities can be given as

$$\nabla p \cdot \nabla \mathbf{B} > 0 \tag{2.2}$$

Consequently, the curvature type instabilities are only found in places where both the pressure gradient and the magnetic field gradient point in the same direction. In tokamaks, this condition is met only on the outboard i.e., the Low Field Side (LFS) of the tokamak, but it is possible for this condition to be met at multiple places in a stellarator. Figure (7) shows how these curvature type instabilities are driven. The images show two different scenarios, on the the LFS of the tokamak, and the High Field Side (HFS) of the tokamak. The regions of high pressures are displayed in dark blue, and conversely for the regions of low pressure. As curved magnetic fields are present in this scenario, the ions and electrons experience a drift in the vertical direction but in opposite directions. Due to a pressure gradient, this creates an accumulation of charges on the boundary between the two regions

(first image in figure 7), which in turn creates an electric field and an $\mathbf{E} \times \mathbf{B}$ drift (second image in figure 7).

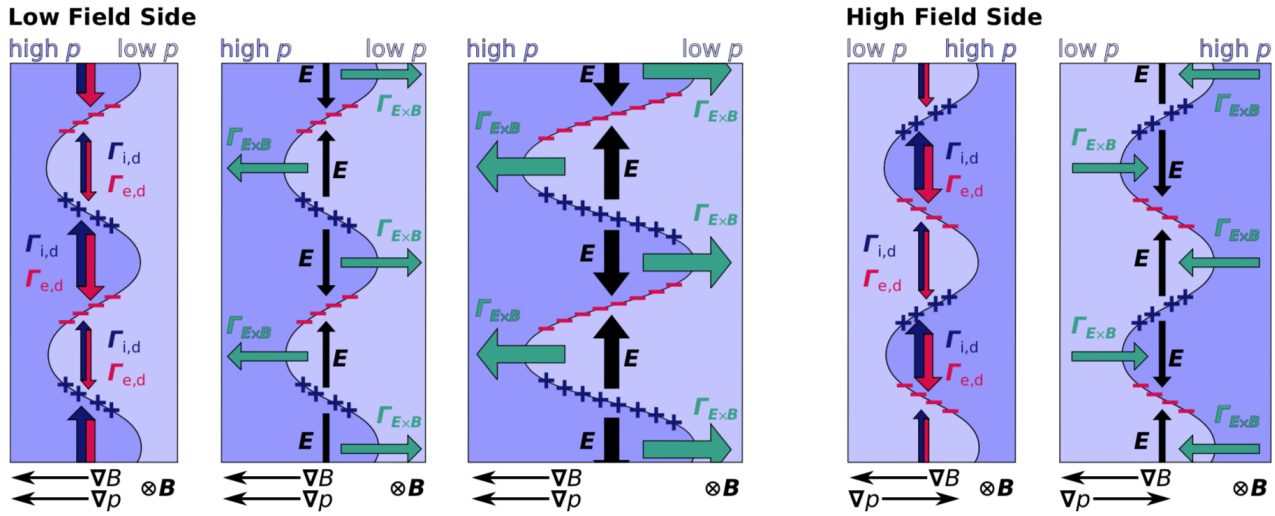


Figure 7: The image describes two different scenarios, to illustrate how microinstabilities are driven, on the LFS and the HFS. The instability criterion as described by equation (2.2) is only met on the LFS. Image Source: Mr. O. Linder

This initial perturbation is reinforced when charge independent fluxes given by

$$\Gamma_{\mathbf{E}\times\mathbf{B}} = n\frac{\mathbf{E}\times\mathbf{B}}{B^2} \tag{2.3}$$

where n is the particle density. These ($\mathbf{E} \times \mathbf{B}$) drifts transport plasma from regions of higher pressure into regions of lower pressure, and similarly transporting plasma from regions of lower pressure into regions of higher pressure (third image in figure 7). Following a similar argument, we can also see that the instabilities are stabilised on the HFS. The perturbations on the HFS cause the $\mathbf{E} \times \mathbf{B}$ drifts to transport plasma into their respective regions, stabilising the instability (last two images in figure 7).

There are four branches of electrostatic microinstabilities that exist, the Ion Temperature Gradient mode (ITG), Electron Temperature Gradient (ETG), Trapped Ion Mode (TIM), and the Trapped Electron Mode (TEM). But TIMs can be ignored as they are suppressed by other nonlinear effects (LaQuey et al., 1975; Cohen et al., 1976). For a given toroidal geometry, several branches of instabilities can potentially be unstable. As shown by figure (3), the instability of the branches depends on the gradients that exist in the system. It shows that no branch is unstable at lower gradients, however, branches are driven unstable past the critical gradient. We also notice that TEMs are primarily driven unstable due to density gradients.

If we consider the same situation as the one considered in figure (7) on the HFS, we can say that the particles will experience a perpendicular drift in the poloidal (perpendicular) direction due to the magnetic curvature drift for example. For passing particles, the parallel velocity is so large that the perpendicular drifts are averaged out while travelling around the torus. However, the perpendicular drift does not average out for trapped particles. Therefore, the trapped electron mode can simply be described as a drift wave that has been driven unstable.

## 2.2 An Outline of the Gyrokinetic Equation

Turbulence is driven by pressure gradients, which results in a change in the distribution function of particles, such as their density, temperature, momentum, and flux. In order to predict plasma turbulence, the 6D Fokker-Planck equation,

$$\frac{\partial f_a}{\partial t} + \mathbf{v}\cdot\nabla_{\mathbf{x}} f_a + \frac{e_a}{m_a}(\mathbf{E}+\mathbf{v}\times\mathbf{B})\cdot\nabla_{\mathbf{v}} f_a = C_a(f_a) \tag{2.4}$$

needs to be solved for each species, where $m_a$ and $e_a$ are the mass and charge of the particle species 'a', $C_a$ is the collisional operator that describes small scale Coulomb interactions between particles species denoted by 'a', and $f_a$ is the particle distribution function (Maxwellian) (Barnes, 2009), which when integrated about the velocity space gives density.

$$n_a = \int f_a d\mathbf{v} \tag{2.5}$$

As long as the potential energy of nearest neighbour interaction is much less than the kinetic energy of the particles, the Fokker-Planck equation describes the full range of dynamics in a six dimensional phase space and time for particles of species 'a' moving in a self-consistent electromagnetic field. However, it does not take into account the effect of external sources of particles.

The 6D Fokker-Planck equation, as it stands, results in a major practical issue, when it comes to the simulation of fusion plasmas. The spatio-temporal scales in fusion plasmas span an enormous range of orders, this makes it practically infeasible to simulate all phenomena in a tractable time-scale.

Gyrokinetics aims to solve the temporal issue by reducing the Fokker-Planck equation to a 5D problem, which is a lot easier to solve when compared to the previous 6D problem. It achieves this by eliminating the fast cyclotron time scale, as most interesting turbulent phenomena occur at much slower time scales. The procedure to achieve this is, at its core, a change of coordinates. That leaves three coordinates to describe the gyro-centre, one for the velocity that is parallel to the background magnetic field, and one for the magnetic moment, an adiabatic invariant which effectively describes the velocity perpendicular to the magnetic field. This leads on to the generalised gyro-kinetic equation (Garbet et al., 2010; Barnes, 2009). The gyrokinetic equation and the quasi-neutrality condition is derived here following the methodology set out in Proll (2014) and elements taken from Cowley (2018).

To begin the outline, we now consider a magnetised plasma where we know that charged particles will gyrate about a magnetic field line with the gyro-radius given by

$$\rho_a = \frac{\sqrt{2m_a T_a}}{e_a B} \tag{2.6}$$

where $T_a$ is the temperature.

One of the key assumptions to be made is that $\epsilon \equiv \rho_a / L << 1$, where L is the typical scale length of the plasma. It is safe to assume this in most magnetically confined plasmas. It is also assumed that

$$\frac{\omega}{\Omega_a} \sim \frac{\rho_a}{L} \sim \frac{\delta n_a}{n_0} \sim \mathcal{O}(\epsilon) \tag{2.7}$$

where $\omega$ is the mode frequency, $\Omega_a$ is the cyclotron frequency, $\delta n_a$ is the density perturbation, and $n_0$ is the initial density (Garbet et al., 2010).

To progress, some convenient variables are defined below.

$$\varepsilon = \frac{m_a v^2}{2} + e_a \phi \tag{2.8}$$

is the energy, composed of both the kinetic and the electrostatic potential energy.

$$\mu = \frac{m_a v_\perp^2}{2B} \tag{2.9}$$

is the magnetic moment, and

$$\mathbf{R} = \mathbf{r} + \frac{\hat{\mathbf{b}} \times \mathbf{v}}{\Omega_a} \tag{2.10}$$

is the position of the gyro-centre (figure 8). Here $\hat{\mathbf{b}}$ is the unit vector along the magnetic field, and $\Omega_a$ is the cyclotron frequency. This is sometimes called the Catto Transformation, after its inventor (Catto, 1978).

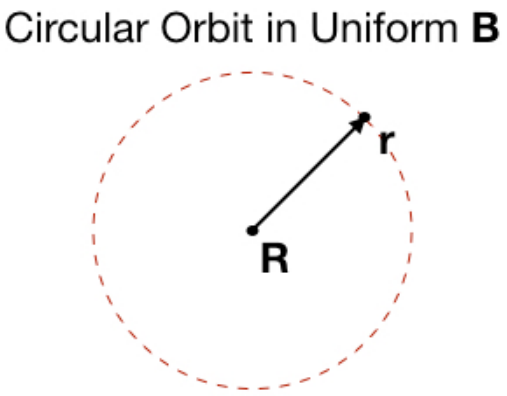


Figure 8: A description of the gyro-centre, where $\mathbf{R}$ is the gyro-centre, and $\mathbf{r}$ is the position of the particle. Image inspired by Cowley (2018)

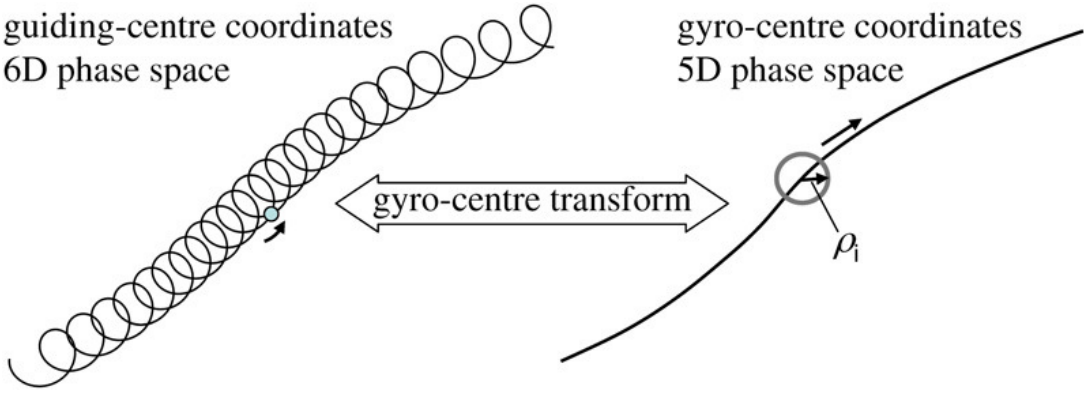


Figure 9: We can eliminate the fast cyclotron time scale by applying the gyro-centre transform, and the problem is reduced from 6D to 5D while keeping kinetic effects such as the finite larmor radius effects (Garbet et al., 2010). Reduces the trajectory of the particle to 'discs' centred about the gyrocentre of the radius $\rho$, given by equation 2.6.

Depending on the system we are trying to describe, we can change the collisional operator to suit our needs. Equation (2.4) would be called the Fokker-Planck equation if the dominant collisional process in the plasma being described is via the Coulomb interactions. In that case, $C_a$ would be the Fokker-Planck operator. However, in most fusion plasmas (very hot plasmas) the frequency of collision is very small. So we can get away with assuming $C_a = 0$, which then makes equation (2.4) the Vlasov equation. If we choose to change the coordinates, and use $\vartheta$ as the gyro-angle, the Vlasov equation can be written as,

$$\frac{\partial f_a}{\partial t} + \dot{\mathbf{R}} \cdot \frac{\partial f_a}{\partial \mathbf{R}} + \dot{\vartheta}\frac{\partial f_a}{\partial \vartheta} + \dot{\varepsilon}\frac{\partial f_a}{\partial \varepsilon} + \dot{\mu}\frac{\partial f_a}{\partial \mu} = 0 \tag{2.11}$$

By noting that $\dot{\vartheta} \simeq -\Omega_a$ and that $m\dot{\mathbf{v}} = e_a(\mathbf{E} + \mathbf{v} \times \mathbf{B})$, we get

$$\dot{\varepsilon} = e_a \left(\frac{\partial \phi}{\partial t}\right)_{\mathbf{r}} \tag{2.12}$$

We then decompose the distribution function as

$$f_a = f_{a0} + g_a + ... \tag{2.13}$$

where $g_a$ is the non-adiabatic part of the distribution function, and $f_{a0}$ is defined as a Maxwellian given by,

$$\begin{aligned} f_{a0} &= n_a(\psi)\left(\frac{m_a}{2\pi T_a(\psi)}\right)^{3/2}\exp\left\{\frac{-\varepsilon}{T_a(\psi)}\right\} \\ &\simeq n_a(\psi)\left(\frac{m_a}{2\pi T_a(\psi)}\right)^{3/2}\exp\left\{\frac{-m_a v^2}{2T_a(\psi)}\right\}\left(1-\frac{e_a\phi}{T_a}\right) \end{aligned} \tag{2.14}$$

where $\psi$ is the flux surface label, and $e_a\phi/T_a << 1$. The adiabatic response is captured within $f_{a0}$. We can also say that $g_a << f_{a0}$.

$$\frac{\partial f_{a0}}{\partial t}+\frac{\partial g_a}{\partial t}+\dot{\mathbf{R}}\cdot\frac{\partial}{\partial\mathbf{R}}(f_{a0}+g_a)-\Omega_a\frac{\partial g_a}{\partial\vartheta}+e_a\left(\frac{\partial\phi}{\partial t}\right)_{\mathbf{r}}\frac{\partial f_{a0}}{\partial\varepsilon}+\dot{\mu}\frac{\partial f_{a0}}{\partial\mu}=0 \tag{2.15}$$

where it is assumed that the lowest order of the distribution function is independent of the gyro-angle.

We can now see that the distribution function is independent of both time, and the magnetic moment. But also that $\partial f_{a0}/\partial\varepsilon = -f_{a0}/T_a$.

$$\frac{\partial g_a}{\partial t}+\dot{\mathbf{R}}\cdot\frac{\partial}{\partial\mathbf{R}}(f_{a0}+g_a)-\Omega_a\frac{\partial g_a}{\partial\vartheta}+\frac{e_a}{T_a}\left(\frac{\partial\phi}{\partial t}\right)_{\mathbf{r}}f_{a0}=0 \tag{2.16}$$

At fixed $\mathbf{R}$, we can now perform a gyro-averaging (equation 2.17) to describe the motion of the gyro-centre ($\mathbf{R}$). Here the integration is carried by also keeping a constant $\mu$ and $\varepsilon$. This is essentially an average over the 'disc' (as shown in figure 9) centred about $\mathbf{R}$.

$$\langle f(\mathbf{v},\mathbf{r},t,...)\rangle_{\mathbf{R}}=\frac{1}{2\pi}\int_0^{2\pi}f\left(\mathbf{v},\mathbf{r},t,...\right)d\vartheta \tag{2.17}$$

If we expand $g_a$ as $g_a = g_{a0}+g_{a1}$, by deducing that $\Omega_a\frac{\partial g_a}{\partial\vartheta}$ is the largest term in equation (2.16), we can approximate $\Omega_a\frac{\partial g_{a0}}{\partial\vartheta}=0$.

$$\frac{\partial g_{a0}}{\partial t}+\langle\dot{\mathbf{R}}\rangle_{\mathbf{R}}\cdot\frac{\partial}{\partial\mathbf{R}}(f_{a0}+g_a)+\frac{e_a}{T_a}\left\langle\left(\frac{\partial\phi}{\partial t}\right)_{\mathbf{r}}\right\rangle_{\mathbf{R}}f_{a0}=0 \tag{2.18}$$

$$\langle\dot{\mathbf{R}}\rangle_{\mathbf{R}}=v_\parallel\hat{\mathbf{b}}+\mathbf{v}_E+\mathbf{v}_{da} \tag{2.19}$$

where $\mathbf{v}_E$ is given by

$$\mathbf{v}_E=\frac{\hat{\mathbf{b}}\times\nabla\langle\phi\rangle_{\mathbf{R}}}{B} \tag{2.20}$$

is the ExB drift velocity, and $\mathbf{v}_{da}$ given by

$$\mathbf{v}_{da}=\frac{\hat{\mathbf{b}}}{2\Omega_a}\times\left(v_\perp^2\nabla lnB+v_\parallel^2\boldsymbol{\kappa}\right) \tag{2.21}$$

is the magnetic drift velocity, and $\boldsymbol{\kappa}=\hat{\mathbf{b}}\cdot\nabla\hat{\mathbf{b}}$ which is the curvature component.

$$\frac{\partial g_{a0}}{\partial t}+(v_\parallel\hat{\mathbf{b}}+\mathbf{v}_E+\mathbf{v}_{da})\cdot\nabla g_{a0}+(\mathbf{v}_E+\mathbf{v}_{da})\cdot\nabla f_{a0}-\frac{e_a}{T_a}\left\langle\left(\frac{\partial\phi}{\partial t}\right)_{\mathbf{r}}\right\rangle_{\mathbf{R}}f_{a0}=0 \tag{2.22}$$

Here, we can ignore $\mathbf{v}_E\cdot\nabla g_{a0}$ as it is non-linear in its fluctuations, and $\mathbf{v}_{da}\cdot\nabla f_{a0}$ as is gives the neoclassical response in $g_{a0}$ which simply adds to the fluctuations driven by the last two terms.

In addition to which, since we know that fluctuations vary slowly along the field lines and rapidly across them, it is convenient to write the perturbed quantities such as $\phi$ or $g_{a0}$ in terms of a slowly varying amplitude and a fast varying phase,

$$\phi(\mathbf{r},t)=\hat{\phi}(\mathbf{r},\omega)\exp\left\{\frac{iS(\mathbf{r})}{\delta-\omega t}\right\} \tag{2.23}$$

$$g_{a0}(\mathbf{R},\varepsilon,\mu,t) = \hat{g}_a(\mathbf{R},\varepsilon,\mu)\exp\left\{\frac{iS(\mathbf{R})}{\delta-\omega t}\right\} \tag{2.24}$$

where $S(\mathbf{r})$ is an eikonal (Cooper et al., 1996), which is assumed to satisfy $B\cdot\nabla S = 0$ so as to guarantee that the modes vary slowly along the magnetic field line (Cooper, 1988). $\hat{\phi}(\mathbf{r})$, $\hat{g}_a(\mathbf{R})$, $S(\mathbf{R})$, and $S(\mathbf{r})$ are assumed to vary on the long (equilibrium) spatial scale, and the fast variation is found in the phase factor. These results are obtained from the Ballooning formalism, which is simply assumed and will not be explored any further as it is outside the scope of this work.

Using the ballooning formalism it is possible to write

$$\left\langle\left(\frac{\partial\phi}{\partial t}\right)_{\mathbf{r}}\right\rangle_{\mathbf{R}} = -i\omega J_0\left(\frac{k_\perp v_\perp}{\Omega_a}\right)\phi(\mathbf{R},t) \tag{2.25}$$

where $J_0$ is a Bessel function of the zeroth order.

If we now represent the magnetic field in Clebsch coordinate representation as

$$\mathbf{B} = \nabla\psi\times\nabla\alpha$$

where $\psi$ is the flux surface label, and $\alpha$ is the magnetic field line label, and the perpendicular wave vector can be written as

$$\mathbf{k}_\perp = k_\psi\nabla\psi + k_\alpha\nabla\alpha$$

Using this coordinate transformation, we can now say that

$$-\mathbf{v}_E\cdot\nabla f_{a0} = iJ_0\left(\frac{k_\perp v_\perp}{\Omega_a}\right)\frac{e_a\phi}{T_a}\omega_{*a}^T f_{a0} \tag{2.26}$$

where $\omega_{*a}^T$, the velocity dependant drift frequency is given by

$$\omega_{*a}^T = \omega_{*a}\left[1+\eta_a\left(\frac{\varepsilon}{T_a}-\frac{3}{2}\right)\right] \tag{2.27}$$

and $\omega_{*a}$, the diamagnetic drift frequency is given by

$$\omega_{*a} = \frac{T_a k_\alpha}{e_a}\frac{dlnn_a}{d\psi} \tag{2.28}$$

and finally $\eta_a$, is the ration between the temperature gradient to the density gradient.

$$\eta_a = \frac{dln(T_a)}{d\psi}\Big/\frac{dln(n_a)}{d\psi} \tag{2.29}$$

By combining all of these terms, we obtain the gyrokinetic relation.

$$v_\parallel\nabla_\parallel\hat{g}_a - i(\omega-\omega_{da})\hat{g}_a = -\frac{ie_a}{T_a}J_0\hat{\phi}(\omega-\omega_{*a}^T)f_{a0} \tag{2.30}$$

where $\omega_{da} = \mathbf{k}_\perp\cdot\mathbf{v}_{da}$.

As the dependence of $\hat{g}_a$ and $\hat{\phi}$ in frequency, and their slow variation in space is implied, we can now drop the hats.

$$v_\parallel\nabla_\parallel g_a - i(\omega-\omega_{da})g_a = -\frac{ie_a}{T_a}J_0\phi(\omega-\omega_{*a}^T)f_{a0} \tag{2.31}$$

Due to the low mass of the electrons, they tend to move very quickly along the magnetic field line, therefore we can say that the first term is dominant. If we then expand $g_a = g_{a0}+g_{a1}+...$ with $g_{a1} << g_{a0}$, in the lowest order we find that $\nabla_\parallel g_{a0} = 0$.

If the gyrokinetic equation (2.31) is divided by $v_\parallel$ and integrated along the field line, we obtain

$$\frac{\oint \frac{dl}{v_\parallel}(v_\parallel \nabla_\parallel g_{a0} - i(\omega - \omega_{da})g_{a0})}{\oint \frac{dl}{v_\parallel}} = \frac{\oint \frac{dl}{v_\parallel}\left(-\frac{ie_a}{T_a}J_0\phi(\omega - \omega^T_{*a})f_{a0}\right)}{\oint \frac{dl}{v_\parallel}} \tag{2.32}$$

where the equation has been divided by $\oint \frac{dl}{v_\parallel}$ for normalisation. This operation can be written as,

$$\overline{f} = \frac{2}{\tau_b}\int_{l_1}^{l_2} f \frac{dl}{|v_\parallel|} \tag{2.33}$$

which can be described as a bounce averaging for trapped particles. Here, $l_1$ and $l_2$ are the bounce points for the particle (figure 10), and $\tau_b$ is the bounce time, given by

$$\tau_b = 2\int_{l_1}^{l_2} \frac{dl}{|v_\parallel|} \tag{2.34}$$

where $v_\parallel$ is the parallel velocity of the particle.

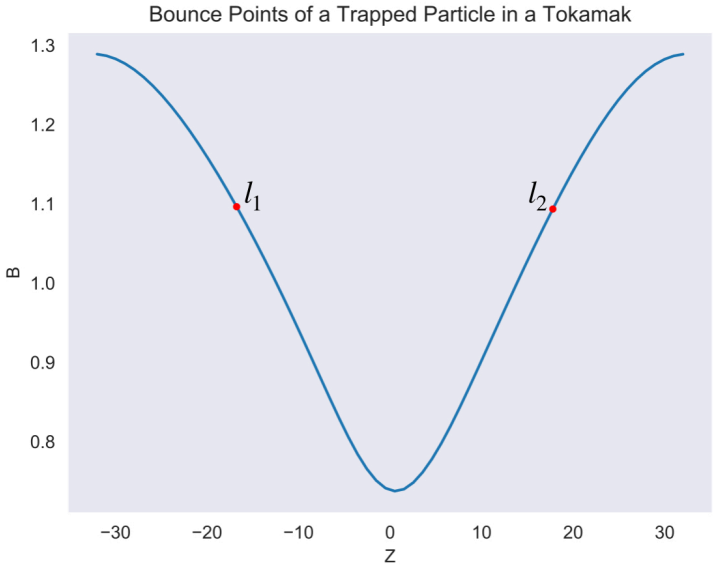


Figure 10: The figure shows a helical field line within a Tokamak, where a particle is bouncing between the two bounce points $l_1$ and $l_2$. These points are determined by the parallel velocity that the particle is carrying, and the magnetic field strength of the Tokamak.

It can be proven that $\overline{v_\parallel \nabla_\parallel g_{a0}} = 0$, for both passing and trapped particles (Proll, 2014). We also know that only $\omega_{da}$, $\phi$, and $J_0$ vary along the field line, so we can write equation (2.32) as

$$(\omega - \overline{\omega}_{da})g_{a0} = \frac{e_a}{T_a}\overline{J_0\phi}(\omega - \omega^T_{*a})f_{a0} \tag{2.35}$$

When equation (2.35) is re-arranged, we obtain the solution for fast moving particles along the field line ($\omega << k_\parallel v_{T_a}$).

$$g_a = \frac{e_a}{T_a}\overline{J_0\phi}\frac{(\omega - \omega^T_{*a})}{(\omega - \bar{\omega_{da}})}f_{a0} \tag{2.36}$$

We can now re-visit TEM theory where, one of the more important factors to be considered is the local radial curvature. We know from Proll et al. (2015) that

$$\overline{\omega}_{de}\omega_{*e} > 0 \tag{2.37}$$

is a criteria for the electrons to have a destabilising effect on the TEM, where $\overline{\omega}_{de}$ is the magnetic drift frequency averaged over the magnetic field line, and $\omega_{*e}$ is the diamagnetic drift frequency (Proll et al., 2015).

In figure (4) we see regions where $\kappa$ is positive, and regions where it is negative. Figure (11) shows a stable scenario where the two frequencies are in the opposite directions. $\overline{\omega}_{de}(\propto \kappa)$ must be negative (as $\omega_{*e} \propto dn/dr$ is negative by definition), if TEMs are to be driven unstable. Such regions, where the particle mainly sees negative curvature is called a 'bad curvature region', and vice-versa.

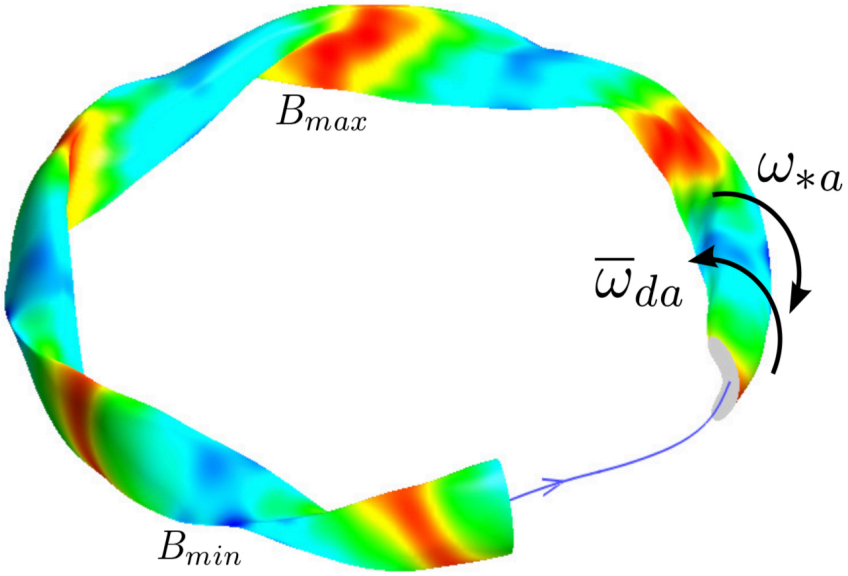


Figure 11: The image shows the magnetic field strength of the quasi-isodynamic stellarator QIPC (Subbotin et al., 2006; Proll, 2014). While the arrows indicate the directions of the diamagnetic drift frequency, and the bounce averaged magnetic drift frequency.

### 2.3 Quasi-neutrality

We will now introduce quasi-neutrality by using the poisson equation to close our system of equations.

$$\nabla^2 \varphi = \frac{e^2(n_e - n_i)}{\epsilon_0 T_0} \tag{2.38}$$

where $\varphi = e\phi/T_0$, $n_e$ and $n_i$ are the electron and ion densities, and $T_0$ is the temperature.

We now assume that the electron and ion densities are approximately equal to the density $n_0$, with small perturbations, written as

$$n_a = n_0 + \delta n_a$$

where 'a' denotes the particle species. This leads us to,

$$\nabla^2 \varphi = \frac{\delta n_e - \delta n_i}{n_0 \lambda_D^2} \tag{2.39}$$

where $\lambda_D^2 = \epsilon_0 T_0 / n_0 e^2$, the Debye length.

In fusion plasmas, the Debye length is one of the smallest scale lengths. We also know that the potential varies on a length scale which can be approximated as $\nabla\varphi \sim L$, which gives us

$$\frac{\delta n_e - \delta n_i}{n_0} \sim \left(\frac{\lambda_D}{L}\right)^2 \tag{2.40}$$

If the length scales of the potential are large compared to the Debye length ($L >> \lambda_D$), the density increments must cancel each other to satisfy equation (2.40). Using this information, we can write the quasi-neutrality equation as

$$\sum_a e_a \delta n_a = 0 \tag{2.41}$$

where the density perturbation can be written as

$$\delta n_a(\mathbf{r}, t) = \int_{\mathbf{r}=const} (f_{a0} + g_{a0}) d\mathbf{v} - n_a(\mathbf{r}) \tag{2.42}$$

where,

$$\int f_{a0} d\mathbf{v} = n_a \left(1 - \frac{e_a \phi}{T_a}\right) \tag{2.43}$$

and

$$\int g_{a0} d\mathbf{v} = \exp\left\{\frac{iS(\mathbf{R})}{\delta - \omega t}\right\} \int g_a(\mathbf{R}, \epsilon, \mu) J_0 \left(\frac{k_\perp v_\perp}{\Omega_a}\right) d\mathbf{v} \tag{2.44}$$

which is obtained by using the definition of $g_{a0}$ given by equation (2.24). We would also need to remember that we have dropped the hats because a slow variation in space is implied. Which gives us the quasi-neutrality condition, when we also use the definition of $\phi$ given by equation (2.23).

$$\sum_a \frac{n_a e_a^2}{T_a} \phi = \sum_a e_a \int g_a(\mathbf{R}, \epsilon, \mu) J_0 \left(\frac{k_\perp v_\perp}{\Omega_a}\right) d\mathbf{v} \tag{2.45}$$

GENE (Gyrokinetic Electromagnetic Numerical Experiment) (Jenko et al., 2000; Xanthopoulos et al., 2009; Jenko, 2000; Merz, 2008) is a code that can be used to solve the gyrokinetic equations outlined in this chapter. GENE can be used either in a nonlinear or a linear form, both of which have been shown to yield reliable results (Jenko, 2000). The particle distribution function is evaluated in five-dimensional phase space, and includes the calculation of both passing particle and trapped particles. While GENE does have the potential to simulate entire flux surface in a stellarator, the data has been extracted from a flux tube simulation, where a small annulus around a given field line is simulated, and the background density and temperature profiles are assumed to be constant. To simplify calculations, a flat temperature profile can be assumed. This is true of all GENE graphs presented in this work.

GENE treats different geometries by coupling itself to GIST (Geometry Interface for Stellarators and Tokamaks) (Xanthopoulos et al., 2009). This is highly process intensive and takes up to $\approx 10^6$ CPUs (1 CPUs = 1 real time processing second on one CPU) for strong instabilities. However, the calculations can be sped up by process parallelisation across five phase space dimensions as well as across the number of particles considered.

# 3 Derivation of the Dispersion Relation

In order to analyse TEM stability in a plasma and predict the threshold, we will first need to derive a dispersion relation based on the gyrokinetic framework that has been outlined in the previous chapter. It is important to note that the following derivation has been carried out from the perspective of a tokamak, but it is adaptable to stellarators by substituting alternate magnetic geometries. In this chapter, an outline of the initial parameters have been provided, before embarking upon the derivation of the dispersion relation for the TEM.

## 3.1 Outline of Assumptions

We first assume that the frequency of the mode is much smaller than the bounce frequencies of both the ions, and the electrons.

$$\omega << \omega_{bi} << \omega_{be} \tag{3.1}$$

We then assume the non-adiabatic part of the perturbed equation given by 3.2, as passing particles are treated adiabatically. Therefore, the adiabatic part is not included here.

$$g_a = \frac{e_a}{T_a}\overline{J_0\phi}\frac{(\omega - \omega_{*a}^T)}{(\omega - \bar{\omega}_{da})}f_{a0} \tag{3.2}$$

where $\omega_{*a}^T$ is the velocity dependent drift frequency, given by equation (3.3).

$$\omega_{*a}^T = \omega_{*a}\left[1 + \eta_a\left(\frac{\varepsilon}{T_a} - \frac{3}{2}\right)\right] \tag{3.3}$$

where $\omega_{*a}$ is the diamagnetic drift frequency given by,

$$\omega_{*a} = \frac{T_a}{Be_a}\frac{dln(n_a)}{dr}\left(\hat{b}\times\nabla r\right)\cdot\mathbf{k}_\perp \tag{3.4}$$

and $\eta_a$ is the ratio between the temperature gradient and the density gradient, given by

$$\eta_a = \frac{dln(T_a)}{d\psi}\Big/\frac{dln(n_a)}{d\psi} \tag{3.5}$$

We also assume the bounce averaged magnetic drift frequency

$$\overline{\omega}_{da} = \overline{\mathbf{k}_\perp\cdot\mathbf{v}_{da}} \tag{3.6}$$

and the quasi-neutrality condition.

$$\sum_a \frac{n_a e_a^2}{T_a}\phi = \sum_a e_a\int g_a(\mathbf{R},\epsilon,\mu)J_0\left(\frac{k_\perp v_\perp}{\Omega_a}\right)d\mathbf{v} \tag{3.7}$$

In addition to which, the Maxwellian has been assumed to be

$$f_{a0} = n_a(\psi)\left(\frac{m_a}{2\pi T_a(\psi)}\right)^{3/2}\exp\left\{\frac{-m_a v^2}{2T_a(\psi)}\right\} \tag{3.8}$$

Here, as with equation (3.2), only the non-adiabatic part is included.

## 3.2 The Dispersion Relation

To start off, we first consider the quasi-neutrality condition (equation 3.7), and approximate the zeroth order Bessel function ($J_0$) to 1, as we are considering long perpendicular wavelengths ($k_\perp\rho_a << 1$). When equation (3.2) is substituted in equation (3.7), we get

$$\begin{aligned}\sum_a \frac{n_a e_a^2}{T_a}\phi &= \sum_a e_a \int_{trapped} g_a(\mathbf{R},\epsilon,\mu)d\mathbf{v} \\ &= \sqrt{2\epsilon}\sum_a e_a \int_{trapped} \frac{e_a}{T_a}\overline{\phi}\frac{(\omega-\omega_{*a}^T)}{(\omega-\overline{\omega}_{da})} f_{a0}d\mathbf{v} \\ &= \sqrt{2\epsilon}\sum_a e_a \int_{trapped} \frac{e_a}{T_a}\overline{\phi}\frac{(\omega-\omega_{*a}^T)}{(\omega-\overline{\omega}_{da})} f_{a0}d\mathbf{v}\end{aligned} \tag{3.9}$$

where the factor of $\sqrt{2\epsilon}$ denotes the fraction of trapped particles, which is included so as to only for the trapped particles, and $\epsilon$ is the inverse aspect ratio (a/R).

Here, a further approximation is made where we consider that the electrostatic potential does not depend on the position along the field line, which implies that $\phi = \overline{\phi}$. This is quite a brutal approximation, as it does indeed depend on the position along the field line, yet it simplifies the mathematics considerably. It is also important to note that,

$$\int f_{a0}d\mathbf{v} = n_a \tag{3.10}$$

When we implement these approximations in equation (3.9), we get

$$\sum_a \frac{n_a e_a^2}{T_a} = \sqrt{2\epsilon}\sum_a e_a \int_{trapped} \frac{e_a}{T_a}\frac{(\omega-\omega_{*a}^T)}{(\omega-\overline{\omega}_{da})} f_{a0}d\mathbf{v} \tag{3.11}$$

$$\sum_a \frac{n_a e_a^2}{T_a} = \sqrt{2\epsilon}\sum_a \frac{e_a^2}{T_a}\frac{(\omega-\omega_{*a})}{(\omega-\tilde{\omega}_{da})} n_a \tag{3.12}$$

where we have effectively fixed the definition of $\tilde{\omega}_{da}$. When following previous works (Proll, 2014), $\overline{\omega}_{da}$ disappears when the integral in equation (3.11) is evaluated with a frequency ordering ($\overline{\omega}_{da} << \omega$). But seeing as curvature is an important component in turbulence studies, $\tilde{\omega}_{da}$ is re-introduced as a reminder of the direction of the curvature.

The exact definition of $\tilde{\omega}_{da}$ can be derived by considering the denominator of equation (3.9), and using the approximation $\overline{\omega}_{da} << \omega$ (and a taylor expansion), to obtain an identity.

$$\begin{aligned}\frac{1}{\omega-\overline{\omega}_{da}} &= \frac{1}{\omega}\left(\frac{\omega-\overline{\omega}_{da}}{\omega}\right)^{-1} \\ &= \frac{1}{\omega}\left(1-\frac{\overline{\omega}_{da}}{\omega}\right)^{-1} \\ &\approx \frac{1}{\omega}\left(1+\frac{\overline{\omega}_{da}}{\omega}+...\right)\end{aligned} \tag{3.13}$$

This is a very crucial ordering approximation, but not entirely accurate. The magnetic drift frequency is typically not that small. However, it is an ordering that needs to be made for the integral to be evaluated at all. By employing this identity in equation (3.11) to obtain

$$\int_{trapped}(\omega-\omega_{*a})\frac{1}{\omega}(1+\frac{\overline{\omega}_{da}}{\omega}+HO)f_{a0}d\mathbf{v} = (\omega-\omega_{*a})\frac{1}{\omega}(1+\frac{\tilde{\omega}_{da}}{\omega}+HO)n_a \tag{3.14}$$

where HO are the higher order terms which will be ignored for this evaluation. Thus, this equality can be evaluated as

$$\tilde{\omega}_{da} = \frac{1}{\left(1-\frac{\omega_{*a}}{\omega}\right)n_a}\left[\int_{tr}\overline{\omega}_{da}f_{a0}d\mathbf{v} - \int_{tr}\frac{\omega_{*a}^T\overline{\omega}_{da}}{\omega}f_{a0}d\mathbf{v}\right] \tag{3.15}$$

We now carry on again from equation (3.12), which can be written as

$$\sum_a\left[\frac{n_a e_a^2}{T_a} - \sqrt{2\epsilon}\frac{e_a^2}{T_a}n_a\frac{(\omega-\omega_{*a})}{(\omega-\tilde{\omega}_{da})}\right] = 0 \tag{3.16}$$

By expanding the summation, and assuming that $n_i = n_e$, we obtain

$$\frac{1}{\sqrt{2\epsilon}}\left(\frac{1}{T_e}+\frac{1}{T_i}\right) = \frac{1}{T_e}\frac{(\omega-\omega_{*e})}{(\omega-\tilde{\omega}_{de})} + \frac{1}{T_i}\frac{(\omega-\omega_{*i})}{(\omega-\tilde{\omega}_{di})} \tag{3.17}$$

We now make the assumption that $T_e = T_i$. We also make the observation that $\omega_{*e} = -\omega_{*i}$ (from equation 3.3), and that $\tilde{\omega}_{de} = -\tilde{\omega}_{di}$ (from equation 4.13).

$$\begin{aligned}\sqrt{\frac{2}{\epsilon}} &= \frac{(\omega-\omega_{*e})}{(\omega-\tilde{\omega}_{de})} + \frac{(\omega+\omega_{*e})}{(\omega+\tilde{\omega}_{de})} \\ \sqrt{\frac{2}{\epsilon}} &= \frac{2\omega^2 - 2\omega_{*e}\tilde{\omega}_{de}}{\omega^2-\tilde{\omega}_{de}^2}\end{aligned} \tag{3.18}$$

Which gives us a dispersion relation of the form,

$$\omega^2(1-\sqrt{2\epsilon}) = (\tilde{\omega}_{de} - \sqrt{2\epsilon}\omega_{*e})\tilde{\omega}_{de} \tag{3.19}$$

which is exactly the one found in Proll (2014).

# 4 Derivation of the Proxy

We now pick up from the dispersion relation that was derived in the previous chapter (equation 3.19). To derive the criterion for instability, we notice that $\omega^2$ can only be imaginary if $\tilde{\omega}_{de}$ and $\omega_{*e}$ have the same sign, and when

$$\sqrt{2\epsilon}\omega_{*e} > \tilde{\omega}_{de} \tag{4.1}$$

is satisfied. Equation (3.19) varies slightly the dispersion relation given in Wesson and Campbell (2011),

$$\omega^2 = \overline{\omega}_{de}(\overline{\omega}_{de} + \sqrt{2\epsilon}\omega_{*e}) \tag{4.2}$$

However, the argument (equation 4.1) is still valid in both versions of the dispersion relation ($\omega_*$ is defined with an extra negative sign in Wesson and Campbell (2011)). Therefore we can be confident with the argument made, and carry on with the derivation by finding the point of marginal stability, which is defined as the point at which the turbulence instability growth rate ($\gamma$) tends to $0^+$, for $\omega = \omega_r + i\gamma$. This point effectively provides us with the critical gradient. This criteria can be written (following on from equation 4.1) as

$$\tilde{\omega}_{de} = \sqrt{2\epsilon}\omega_{*e} \tag{4.3}$$

where

$$\begin{aligned} \omega_{*a} &= \frac{T_a}{Be_a}\left(\hat{b} \times \nabla(n_a)\right) \cdot \mathbf{k}_\perp \\ &= \frac{T_a}{Be_a}\frac{dln(n_a)}{dr}\left(\hat{b} \times \nabla r\right) \cdot \mathbf{k}_\perp \end{aligned} \tag{4.4}$$

is the diamagnetic drift frequency, $\frac{dln(n_a)}{dr}$ is the logarithmic density gradient which in this case is the critical gradient.

$$\begin{aligned} \omega_{da} &= \mathbf{k}_\perp \cdot \mathbf{v}_{da} \\ &= \frac{v_\parallel^2 + v_\perp^2/2}{\Omega_a}\left(\hat{b} \times \boldsymbol{\kappa}\right) \cdot \mathbf{k}_\perp \end{aligned} \tag{4.5}$$

is the magnetic drift frequency, $v_\parallel$ is the parallel velocity of the particle and $v_\perp$ is the perpendicular velocity.

$$\boldsymbol{\kappa} = \nabla lnB = \frac{\nabla B}{B} \tag{4.6}$$

is the curvature.

I will now outline a few more definitions that are required for us to evaluate equation (4.3). The bounce average of a function is given by,

$$v_\parallel = v\sqrt{1 - \lambda B} \tag{4.7}$$

where $v_\parallel$ is the is derived using,

$$v^2 = v_\parallel^2 + v_\perp^2 \tag{4.8}$$

and

$$\lambda = \frac{v_\perp^2}{v^2 B} \tag{4.9}$$

where $\lambda$ is the pitch angle.

We know from Xanthopoulos et al. (2009) that $(\hat{b} \times \boldsymbol{\kappa}) \cdot \mathbf{k}_\perp$ can be boiled down to $\kappa_\alpha k_\alpha$ ($\mathbf{k}_\perp = k_\psi \nabla\psi + k_\alpha \nabla\alpha$), where $\alpha$ is simply the filed line label as given in Clebsch coordinates. We now elaborate on the LHS of equation (4.3) now, from where we left off in equation (4.5). At this point, we will also

re-scale the velocity variable by using $x = \frac{v}{v_{T_a}}$, where $v_{T_a}$ is the thermal velocity of the particle given by $v_{T_a} = \sqrt{\frac{k_B T_a}{m_a}}$.

When these are used in equation (4.5), we get

$$\omega_{da} = (x v_{T_a})^2 \left(1 - \frac{\lambda B}{2}\right) \frac{\kappa_\alpha k_\alpha}{\Omega_a} \tag{4.10}$$

We can now bounce average this relation as defined by equation (2.33), leading to

$$\begin{aligned}
\overline{\omega}_{da} &= (x v_{T_a})^2 \frac{1}{\tau_b} \int_{l_1}^{l_2} \left(1 - \frac{\lambda B(l)}{2}\right) \frac{\kappa_\alpha(l) k_\alpha}{\Omega_a} \frac{dl}{|v_\parallel|} \\
&= (x v_{T_a})^2 \frac{1}{\frac{1}{x v_{T_a}} \int_{l_1}^{l_2} \frac{dl}{\sqrt{1-\lambda B(l)}}} \int_{l_1}^{l_2} \left(1 - \frac{\lambda B(l)}{2}\right) \frac{\kappa_\alpha(l) k_\alpha}{\Omega_e} \frac{dl}{x v_{T_a} \sqrt{1-\lambda B(l)}} \\
&= \frac{(x v_{T_a})^2 \int_{l_1}^{l_2} \frac{\left(1 - \frac{\lambda B(l)}{2}\right)}{\sqrt{1-\lambda B(l)}} \frac{\kappa_\alpha(l) k_\alpha}{\Omega_a} dl}{\int_{l_1}^{l_2} \frac{dl}{\sqrt{1-\lambda B(l)}}}
\end{aligned} \tag{4.11}$$

By now using the full definition of $\tilde{\omega}_{da}$ given by equation (3.14), we now obtain a more verbose form of $\tilde{\omega}_{da}$.

$$\begin{aligned}
\tilde{\omega}_{da} &= \frac{\omega \int_{trapped} \overline{\omega}_{da} f_{a0} d\mathbf{v} - \int_{trapped} \overline{\omega}_{da} \omega_{*a} \left[1 + \eta_a \left(\frac{\varepsilon}{T_a} - \frac{3}{2}\right)\right] f_{a0} d\mathbf{v}}{(\omega - \omega_{*a}) n_a} \\
&= \frac{\omega \int_{trapped} \overline{\omega}_{da} f_{a0} d\mathbf{v} - \omega_{*a} \int_{trapped} \overline{\omega}_{da} f_{a0} d\mathbf{v} - \eta_a \omega_{*a} \int_{trapped} \overline{\omega}_{da} \left(\frac{\varepsilon}{T_a} - \frac{3}{2}\right) f_{a0} d\mathbf{v}}{(\omega - \omega_{*a}) n_a} \\
&= \frac{1}{n_a} \int_{trapped} \overline{\omega}_{da} f_{a0} d\mathbf{v} - \frac{\eta_a \omega_{*a}}{(\omega - \omega_{*a}) n_a} \int_{trapped} \overline{\omega}_{da} \left(\frac{\varepsilon}{T_a} - \frac{3}{2}\right) f_{a0} d\mathbf{v}
\end{aligned} \tag{4.12}$$

Equation (3.15) was expanded as such so that we can separate $\omega_{*a}$ from the first term. Where we can now get rid of the second term by assuming a flat temperature profile ($\eta_a = 0$). This assumption is justified in this case, as all of the simulation data that we will be comparing the proxy to have also assumed a flat temperature profile. It is worth mentioning here that the modes driven unstable by trapped electrons are found to be stable in perfectly quasi-isodynamic (W7-X is a quasi-isodynamic stellarator, albeit not a pefectly quasi-isodynamic stellarator) stellarators while it satisfies the condition $0 < \eta_a < 2/3$, at the electrostatic and collisionless limit (Proll et al., 2012).

$$\tilde{\omega}_{da} = \frac{1}{n_a} \int_{trapped} \overline{\omega}_{da} f_{a0} d\mathbf{v} = \frac{I_1}{n_a} \tag{4.13}$$

where d$\mathbf{v}$ is given by

$$d\mathbf{v} = 2\pi v_\perp dv_\perp dv_\parallel = \sum_\sigma \frac{B\pi v^3 dv d\lambda}{|v_\parallel|} = \sum_\sigma \frac{B\pi (x v_{T_a})^3 v_{T_a} dx d\lambda}{x v_{T_a} \sqrt{1-\lambda B}} \tag{4.14}$$

and $\sigma$ is given by

$$\sigma = \frac{v_\parallel}{v_\parallel} \tag{4.15}$$

As a side note, it is important to remember that

$$\int_{v_1=0}^{v_2=\infty} f_{a0} d\mathbf{v} = n_a \tag{4.16}$$

But getting back to equation (4.13),

$$\begin{aligned}\int_{v_1}^{v_2}\overline{\omega}_{da}f_{a0}d\mathbf{v} &= \int_{x_1}^{x_2}\frac{(xv_{T_a})^2 f_{a0}\int_{l_1}^{l_2}\frac{\left(1-\frac{\lambda B(l)}{2}\right)}{\sqrt{1-\lambda B(l)}}\frac{\kappa_\alpha(l)k_\alpha}{\Omega_e}dl\sum_\sigma\frac{B\pi(xv_{T_a})^3 v_{T_a}dxd\lambda}{xv_{T_a}\sqrt{1-\lambda B}}}{\int_{l_1}^{l_2}\frac{dl}{\sqrt{1-\lambda B}}} \\ &= \frac{2\pi v_{T_a}^5 m_a}{e_a}\int_{x_1}^{x_2}f_{a0}x^4dx\int_{1/B_{max}}^{1/B_{min}}\frac{\int_{l_1}^{l_2}\kappa_\alpha(l)k_\alpha\frac{\left(1-\frac{\lambda B(l)}{2}\right)}{(1-\lambda B(l))}dl}{\int_{l_1}^{l_2}\frac{dl}{\sqrt{1-\lambda B(l)}}}d\lambda\end{aligned} \tag{4.17}$$

where the summation has been reduced to the factor of 2 ($\sum_{\sigma=\pm1}=2$).

This now gives us

$$\tilde{\omega}_{da} = \frac{2\pi v_{T_a}^5 m_a}{n_a e_a}\int_{x_1}^{x_2}x^4 f_{a0}dx\int_{1/B_{max}}^{1/B_{min}}\frac{\int_{l_1}^{l_2}\kappa_\alpha(l)k_\alpha\frac{\left(1-\frac{\lambda B(l)}{2}\right)}{(1-\lambda B(l))}dl}{\int_{l_1}^{l_2}\frac{dl}{\sqrt{1-\lambda B(l)}}}d\lambda \tag{4.18}$$

For the sake of brevity, this shall be written as

$$\tilde{\omega}_{da} = \frac{2\pi v_{T_e}^5 m_a}{n_a e_a}\int_{x_1}^{x_2}...dx\int_{1/B_{max}}^{1/B_{min}}\frac{\int_{l_1}^{l_2}...dl}{\int_{l_1}^{l_2}...dl}d\lambda \tag{4.19}$$

We can now combine this with equation (4.3), and equation (4.4), giving us

$$\frac{2\pi v_{T_e}^5 m_a}{n_e e_e}\int_{x_1}^{x_2}...dx\int_{1/B_{max}}^{1/B_{min}}\frac{\int_{l_1}^{l_2}...dl}{\int_{l_1}^{l_2}...dl}d\lambda = \frac{T_e\sqrt{2\epsilon}}{Be_e}\frac{dln(n_e)}{dr}\left(\hat{b}\times\nabla r\right)\cdot\mathbf{k}_\perp \tag{4.20}$$

where d$\mathbf{v}$ is given by

$$d\mathbf{v} = 2\pi v_\perp dv_\perp dv_\parallel = \sum_\sigma\frac{B\pi v^3 dvd\lambda}{|v_\parallel|} = \sum_\sigma\frac{B\pi(xv_{T_a})^3 v_{T_a}dxd\lambda}{xv_{T_a}\sqrt{1-\lambda B}} \tag{4.21}$$

and $\sigma$ is given by

$$\sigma = \frac{v_\parallel}{|v_\parallel|} \tag{4.22}$$

which captures the direction of travel, of the trapped particle. Hence, the summation can be reduced to the factor of 2 ($\sum_{\sigma=\pm1}=2$).where we have set $\frac{dln(n_e)}{dr}=C_g$, the critical gradient.

We can also simplify the last term on the right hand side of the equation as

$$\begin{aligned}(\hat{b}\times\nabla r)\cdot\mathbf{k}_\perp &= (\frac{\mathbf{B}}{B}\times\nabla\psi)\cdot\mathbf{k}_\perp \\ &= (\frac{\mathbf{B}}{B}\times\nabla\psi)\cdot(k_\psi\nabla\psi+k_\alpha\nabla\alpha) \\ &= (\frac{\mathbf{B}}{B}\times\nabla\psi)\cdot(k_\psi\nabla\psi+k_\alpha\nabla\alpha) \\ &= (\frac{\mathbf{B}}{B}\times\nabla\psi)\cdot(k_\alpha\nabla\alpha) \\ &= (\nabla\psi\times k_\alpha\nabla\alpha)\cdot\frac{\mathbf{B}}{B} \\ &= Bk_\alpha\end{aligned} \tag{4.23}$$

where the definition of the magnetic field in Clebsch coordinates has been used ($\mathbf{B}=\nabla\psi\times\nabla\alpha$), giving us

$$\frac{2\pi v_{T_e}^5 m_a}{n_a e}\int_{x_1}^{x_2} x^4 f_{a0}dx \int_{1/B_{max}}^{1/B_{min}} \frac{\int_{l_1}^{l_2} \frac{\left(1-\frac{\lambda B(l)}{2}\right)}{(1-\lambda B(l))}\kappa_\alpha(l)k_\alpha dl d\lambda}{\int_{l_1}^{l_2}\frac{dl}{\sqrt{1-\lambda B(l)}}} = \frac{T_e\sqrt{2\epsilon}}{Be}C_g B k_\alpha \tag{4.24}$$

$$C_g = \frac{2\pi}{n_e\sqrt{2\epsilon}}\left(\frac{T_e}{m_e}\right)^{3/2}\int_{x_1}^{x_2} x^4 f_{a0}dx \int_{1/B_{max}}^{1/B_{min}} \frac{\int_{l_1}^{l_2} \frac{\left(1-\frac{\lambda B(l)}{2}\right)}{(1-\lambda B(l))}\kappa_\alpha(l)dl}{\int_{l_1}^{l_2}\frac{dl}{\sqrt{1-\lambda B(l)}}} d\lambda \tag{4.25}$$

where the first integral was evaluated to be

$$\int_{x_1}^{x_2} x^4 f_{a0}dx = \int_0^{\infty} x^4 f_{a0}dx = \frac{3n_e m_e^{3/2}}{4\pi T_e^{3/2}} \tag{4.26}$$

giving us the final TEM threshold proxy in the form

$$C_g = \frac{3}{2\sqrt{2\epsilon}}\int_{1/B_{max}}^{1/B_{min}} \frac{\int_{l_1}^{l_2} \frac{\left(1-\frac{\lambda B(l)}{2}\right)}{(1-\lambda B(l))}\kappa_\alpha(l)dl}{\int_{l_1}^{l_2}\frac{dl}{\sqrt{1-\lambda B(l)}}} d\lambda \tag{4.27}$$

# 5 Results

We are finally at a position where we can code in the proxy, and obtain preliminary results that indicate the accuracy of the derived proxy. We will now modify equation (4.27) to include a heaviside function (Proll et al., 2015). This defines the trapped particle region of the magnetic field that is to be considered for the integration of the inner integral. It is equal to unity inside the trapped particle region ($1/B_{max} < \lambda < 1/B_{min}$). Figure (12) shows how the inner integral determines the bounce average for trapped particles characterised by a specific pitch angles. The outer integral then integrates over all such possible cases, to give the threshold.

$$C_g = \frac{3}{2\sqrt{2\epsilon}} \int_{1/B_{max}}^{1/B_{min}} \frac{\int_{l_1}^{l_2} H\left[\frac{1}{\lambda} - B(l)\right] \frac{\left(1-\frac{\lambda B(l)}{2}\right)}{(1-\lambda B(l))} \kappa_\alpha(l) dl}{\int_{l_1}^{l_2} H\left[\frac{1}{\lambda} - B(l)\right] \frac{dl}{\sqrt{1-\lambda B(l)}}} d\lambda \tag{5.1}$$

where $H[f(\lambda, B)]$ denotes a heaviside function.

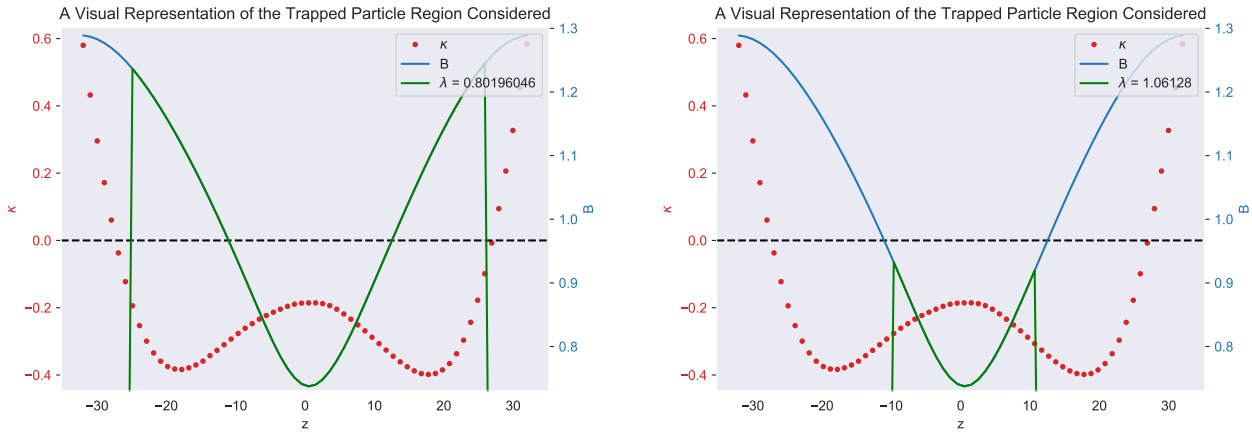


(a) $\lambda = 0.801$ (b) $\lambda = 1.061$

Figure 12: The images display the magnetic field line, and the corresponding curvature of the HSX bean flux tube overlayed on the same graph. In addition to this, the influence of the heaviside function is also plotted. Graph (a) displays what a particle with the pitch angle $\lambda = 0.801$ will see, and correspondingly, graph (b) shows what a particle with the pitch angle $\lambda = 1.061$ will see.

The integrals were implemented in python using the composite trapezoidal rule (Appendix A). The data for $\kappa_\alpha$ was obtained from GIST output files, just like the magnetic field line data, and the data to calculate the inverse aspect ratio ($\epsilon$). When the proxy was calculated for the stellarators and flux tubes in question, it was then compared to the GENE results. However, it is important to note that the conversion from GIST data to $\kappa_\alpha$ is given by

$$\kappa_\alpha = L - \frac{1}{2}\frac{dp/dx}{B} \tag{5.2}$$

where $L$ is the output column in GIST for curvature, and $dp/dx$ is the pressure gradient. As we deal with vacuum configurations, the second term is almost always zero.

Eleven different toroidal devices and flux tubes/magnetic configurations were considered in this part of the study. Below, sets of graphs and images (figure 13 to figure 23) are presented for each of them. The top left shows the curvature on the left axis, and the magnetic field strength on the right axis for multiple stellarators and flux tubes. The data for this graph has been acquired from GIST output files (Xanthopoulos et al., 2009). The top right shows the growth rates of the TEM instability on the y-axis, and the density gradient on the x-axis for multiple stellarators and flux tubes. The results are procured linear runs of GENE. The bottom graph shows the magnetic surface of the relevant device and a cut of the different flux tubes that were analysed.

| Device/Configuration | Flux Tube |
|---|---|
| DIII-D | Midplane |
| HSX | Bean |
| HSX | Triangle |
| W7-X HM | Bean |
| W7-X HM | Triangle |
| W7-X SC | Bean |
| W7-X SC | Triangle |
| W7-X LM | Bean |
| W7-X LM | Triangle |
| NCSX | Bean |
| NCSX | Bullet |

Table 1: The table details all the of the devices, device configurations, and flux tubes used in this study.

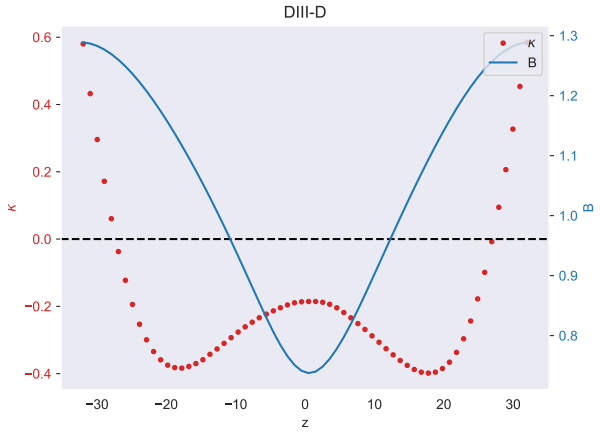


(a) The figure shows the magnetic field line, and the curvature for DIII-D.

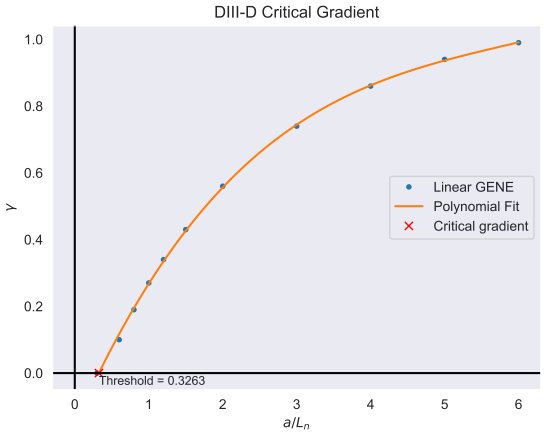


(b) The graph shows the Normalised density gradient v/s the growth rate for DIII-D. It also displays the critical gradient for this geometry.

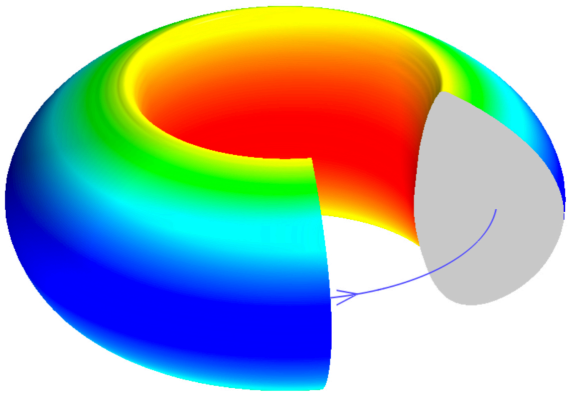

(c) The image shows a magnetic surface plot of DIII-D. The red indicates magnetic maxima, and blue indicates magnetic minima.

Figure 13: The figures above are relevant to DII-D (Luxon, 2002).

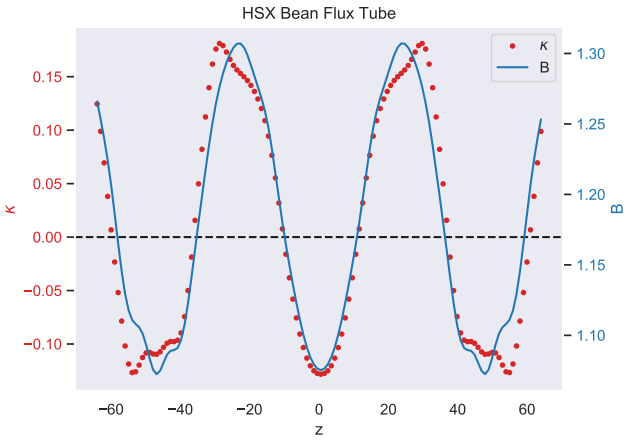


(a) The figure shows the magnetic field line, and the curvature for the bean flux tube in HSX.

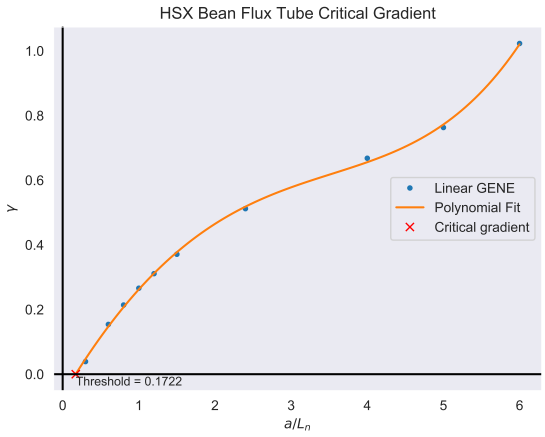


(b) The graph shows the Normalised density gradient v/s the growth rate for the bean flux tube in HSX. It also displays the critical gradient for this geometry.

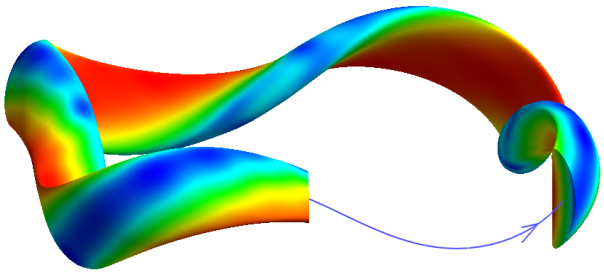

(c) The image shows a magnetic surface plot of HSX, and a cut of the bean flux tube in HSX. The red indicates magnetic maxima, and blue indicates magnetic minima.

Figure 14: The figures above are relevant to the bean flux tube in HSX (Helically Symmetric Experiment). (Almagri et al., 1999)

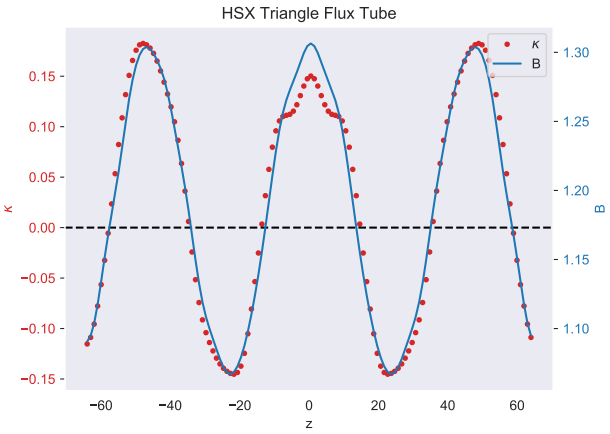


(a) The figure shows the magnetic field line, and the curvature for the triangle flux tube in HSX.

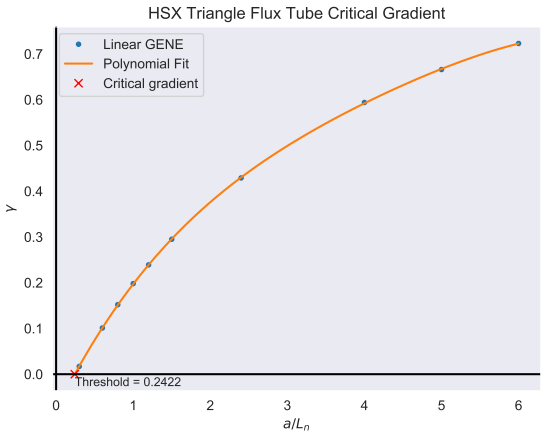


(b) The graph shows the Normalised density gradient v/s the growth rate for the triangle flux tube in HSX. It also displays the critical gradient for this geometry.

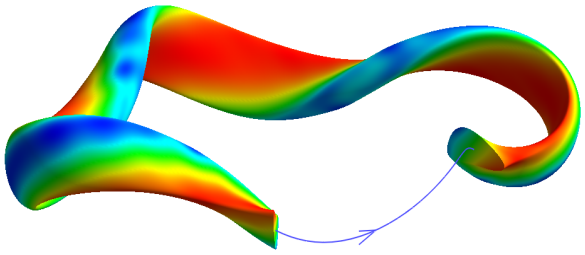

(c) The image shows a magnetic surface plot of HSX, and a cut of the triangle flux tube in HSX. The red indicates magnetic maxima, and blue indicates magnetic minima.

Figure 15: The figures above are relevant to the triangle flux tube in HSX (Helically Symmetric Experiment). (Almagri et al., 1999)

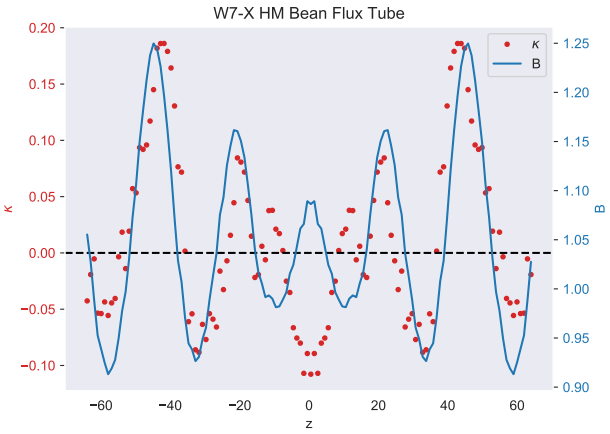


(a) The figure shows the magnetic field line, and the curvature for the bean flux tube in the high mirror configuration of W7-X.

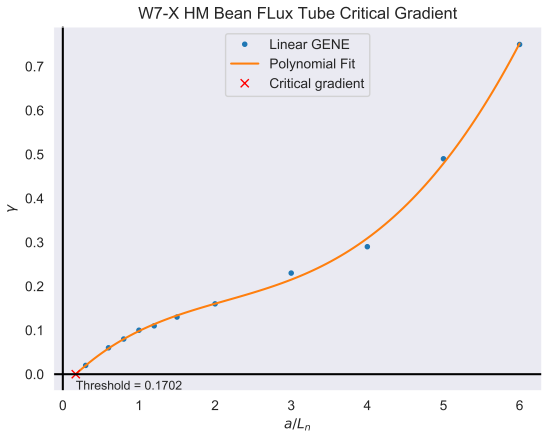


(b) The graph shows the Normalised density gradient v/s the growth rate for the bean flux tube in the high mirror configuration of W7-X. It also displays the critical gradient for this geometry.

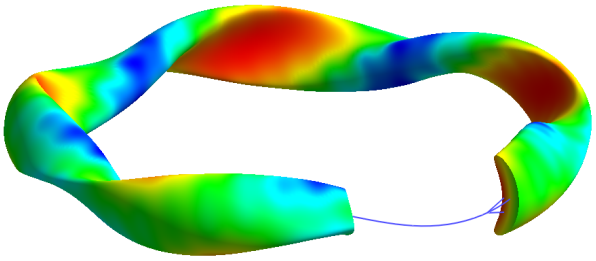

(c) The image shows a magnetic surface plot of W7-X, and a cut of the bean flux tube in the high mirror configuration of W7-X. The red indicates magnetic maxima, and blue indicates magnetic minima.

Figure 16: The figures above are relevant to the triangle flux tube in the High Mirror configuration of W7-X (Wendelstein 7-X) (Nührenberg et al., 1995).

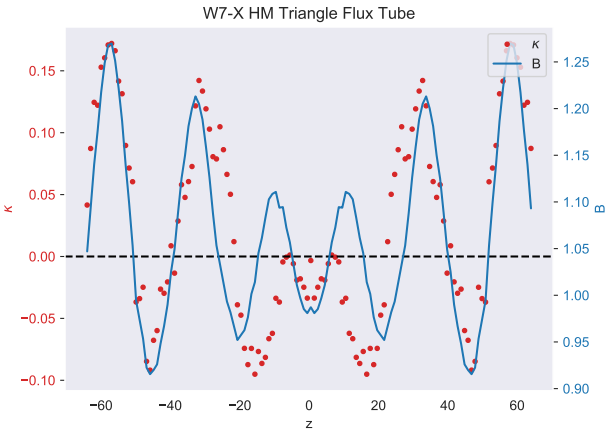


(a) The figure shows the magnetic field line, and the curvature for the triangle flux tube in the high mirror configuration of W7-X.

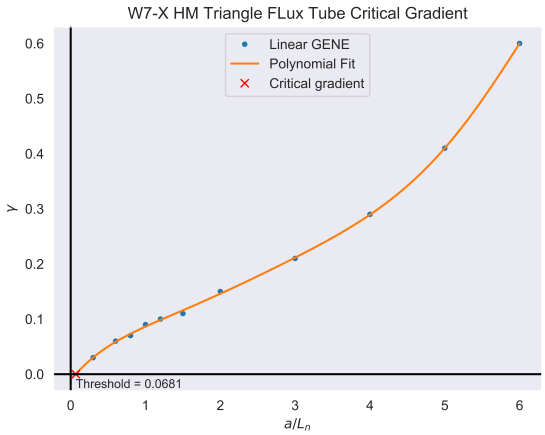


(b) The graph shows the Normalised density gradient v/s the growth rate for the triangle flux tube in the high mirror configuration of W7-X. It also displays the critical gradient for this geometry.

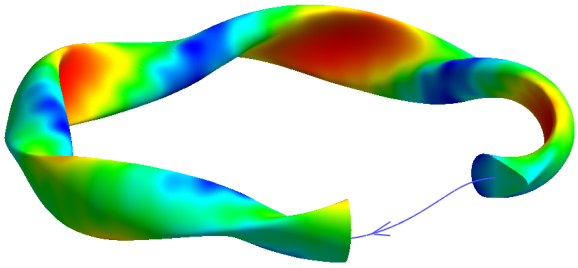

(c) The image shows a magnetic surface plot of W7-X, and a cut of the triangle flux tube in the high mirror configuration of W7-X. The red indicates magnetic maxima, and blue indicates magnetic minima.

Figure 17: The figures above are relevant to the triangle flux tube in the High Mirror configuration of W7-X (Wendelstein 7-X) (Nührenberg et al., 1995).

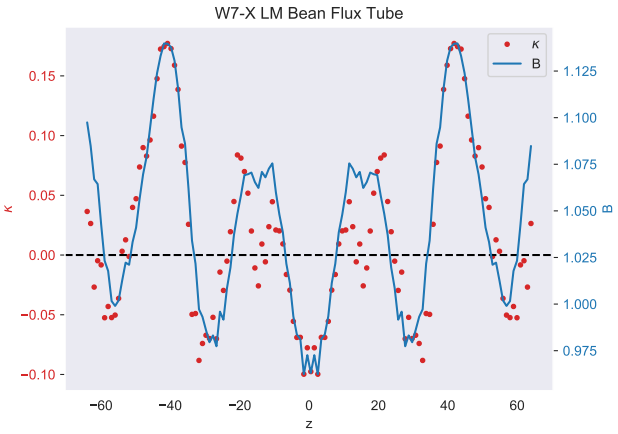


(a) The figure shows the magnetic field line, and the curvature for the bean flux tube in the low mirror configuration of W7-X.

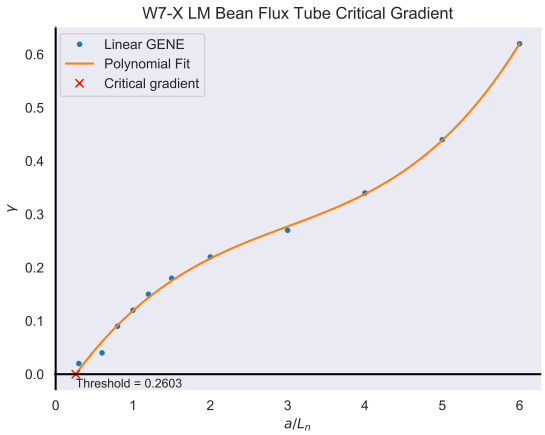


(b) The graph shows the Normalised density gradient v/s the growth rate for the bean flux tube in the low mirror configuration of W7-X. It also displays the critical gradient for this geometry.

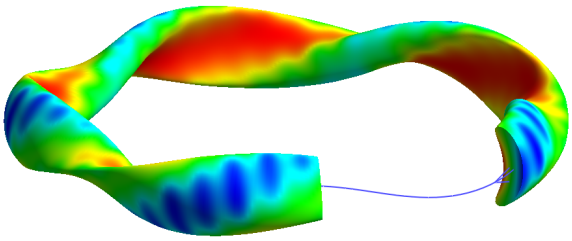

(c) The image shows a magnetic surface plot of W7-X, and a cut of the bean flux tube in the low mirror configuration of W7-X. The red indicates magnetic maxima, and blue indicates magnetic minima.

Figure 18: The figures above are relevant to the bean flux tube in the Low Mirror configuration of W7-X (Wendelstein 7-X) (Nührenberg et al., 1995).

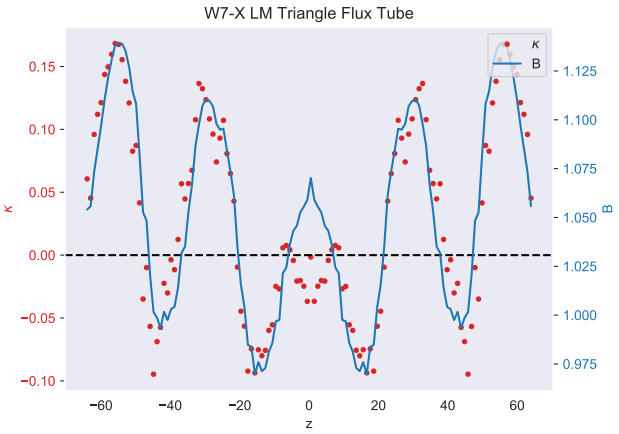


(a) The figure shows the magnetic field line, and the curvature for the triangle flux tube in the low mirror configuration of W7-X.

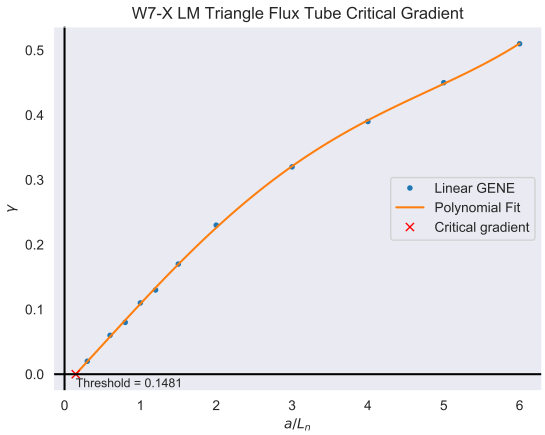


(b) The graph shows the Normalised density gradient v/s the growth rate for the triangle flux tube in the low mirror configuration of W7-X. It also displays the critical gradient for this geometry.

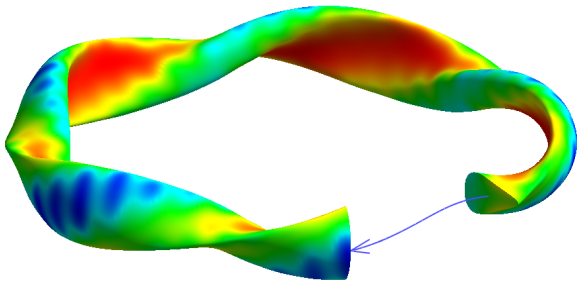

(c) The image shows a magnetic surface plot of W7-X, and a cut of the triangle flux tube in the low mirror configuration of W7-X. The red indicates magnetic maxima, and blue indicates magnetic minima.

Figure 19: The figures above are relevant to the triangle flux tube in the Low Mirror configuration of W7-X (Wendelstein 7-X) (Nührenberg et al., 1995).

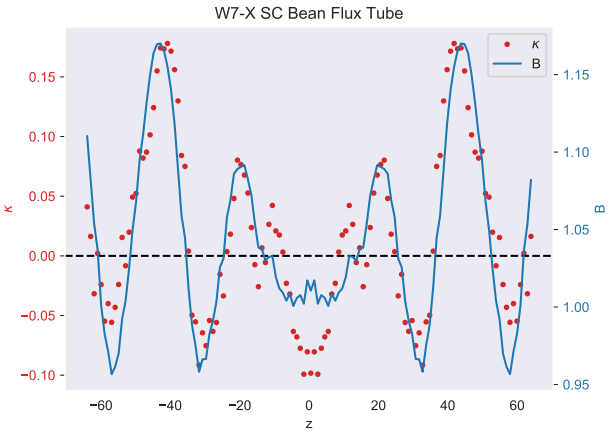


(a) The figure shows the magnetic field line, and the curvature for the bean flux tube in the standard configuration of W7-X.

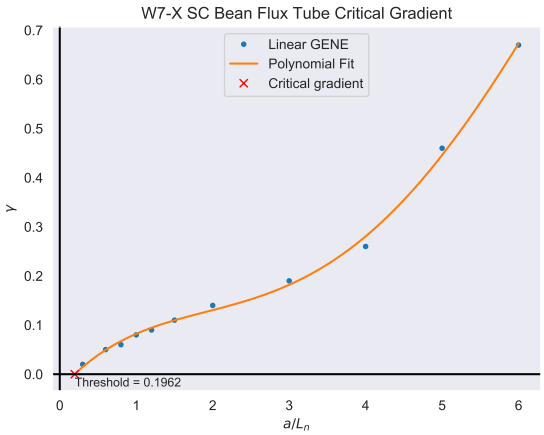


(b) The graph shows the Normalised density gradient v/s the growth rate for the bean flux tube in the standard configuration of W7-X. It also displays the critical gradient for this geometry.

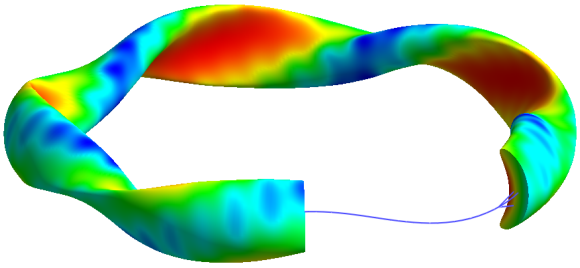

(c) The image shows a magnetic surface plot of W7-X, and a cut of the bean flux tube in the standard configuration of W7-X. The red indicates magnetic maxima, and blue indicates magnetic minima.

Figure 20: The figures above are relevant to the bean flux tube in the Standard Configuration of W7-X (Wendelstein 7-X) (Nührenberg et al., 1995).

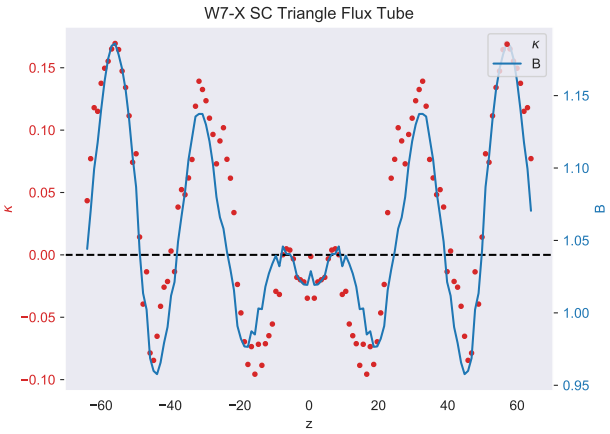


(a) The figure shows the magnetic field line, and the curvature for the triangle flux tube in the standard configuration of W7-X.

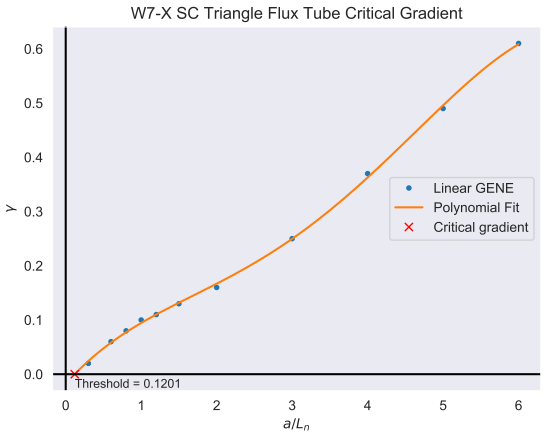


(b) The graph shows the Normalised density gradient v/s the growth rate for the triangle flux tube in the standard configuration of W7-X. It also displays the critical gradient for this geometry.

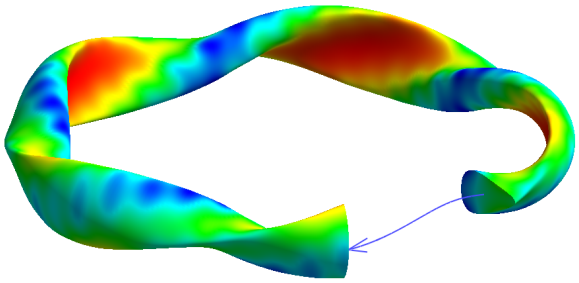

(c) The image shows a magnetic surface plot of W7-X, and a cut of the triangle flux tube in the standard configuration of W7-X. The red indicates magnetic maxima, and blue indicates magnetic minima.

Figure 21: The figures above are relevant to the triangle flux tube in the Standard Configuration of W7-X (Wendelstein 7-X) (Nührenberg et al., 1995).

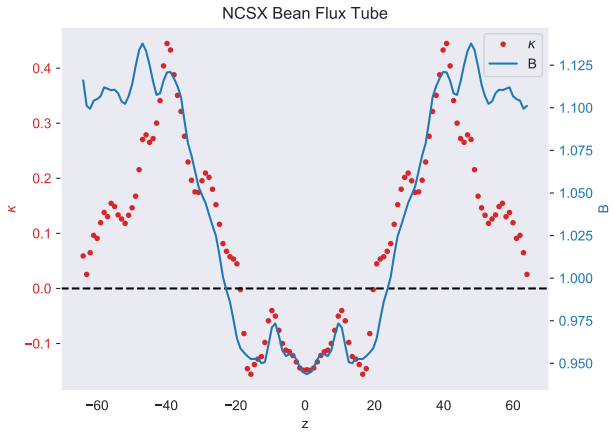


(a) The figure shows the magnetic field line, and the curvature for the bean flux tube in NCSX.

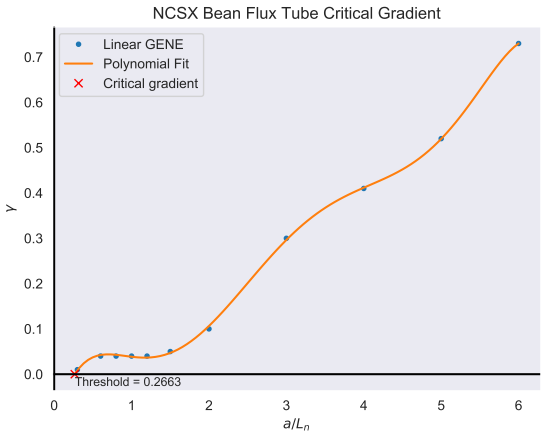


(b) The graph shows the Normalised density gradient v/s the growth rate for the bean flux tube in NCSX. It also displays the critical gradient for this geometry.

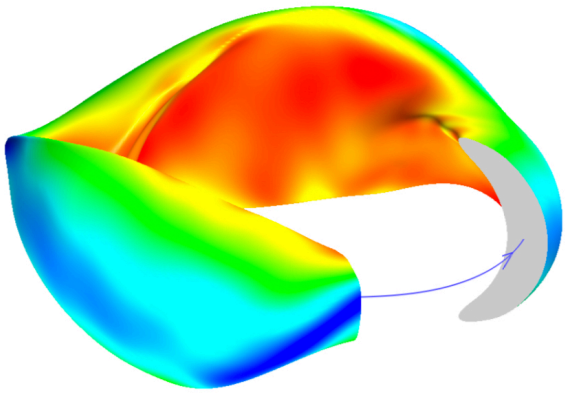

(c) The image shows a magnetic surface plot of NCSX, and a cut of the bean flux tube in NCSX. The red indicates magnetic maxima, and blue indicates magnetic minima.

Figure 22: The figures above are relevant to the bean flux tube in NCSX (National Compact Stellarator Experiment) (Zarnstorff et al., 2001).

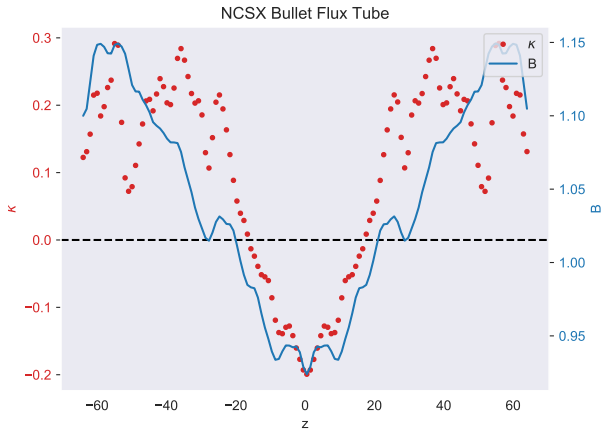


(a) he figure shows the magnetic field line, and the curvature for the bullet flux tube in NCSX.

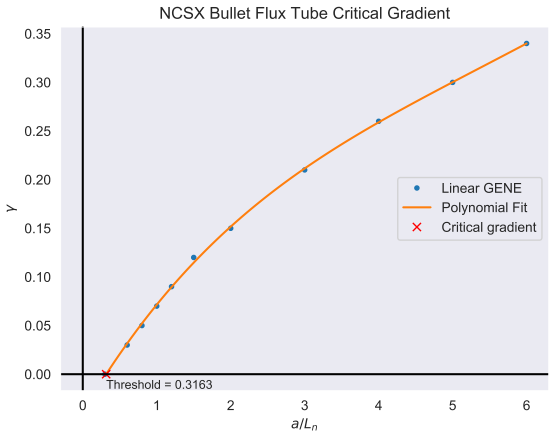


(b) he graph shows the Normalised density gradient v/s the growth rate for the bullet flux tube in NCSX. It also displays the critical gradient for this geometry.

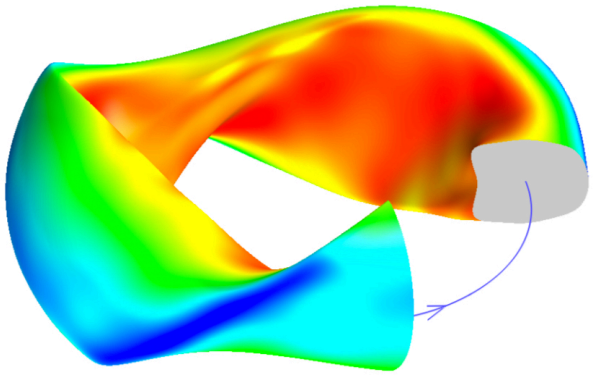

(c) The image shows a magnetic surface plot of NCSX, and a cut of the bullet flux tube in NCSX. The red indicates magnetic maxima, and blue indicates magnetic minima.

Figure 23: The figures above are relevant to the bean flux tube in NCSX (National Compact StellaratorExperiment) (Zarnstorff et al., 2001).

By using the data and methods mentioned in this chapter, the thresholds were calculated. Once the results from the proxy were obtained, they were compared to the threshold data as calculated by GENE, and plotted against each other (figure 24). To do so, $C_g$ was converted to $a/L_{n,proxy}$ by multiplying it with '$-a$' (minor radius). However, DIII-D was omitted from figure (24) as it was off-scale. A table (table 2) is given to provide more detail. The results are discussed in the next chapter.

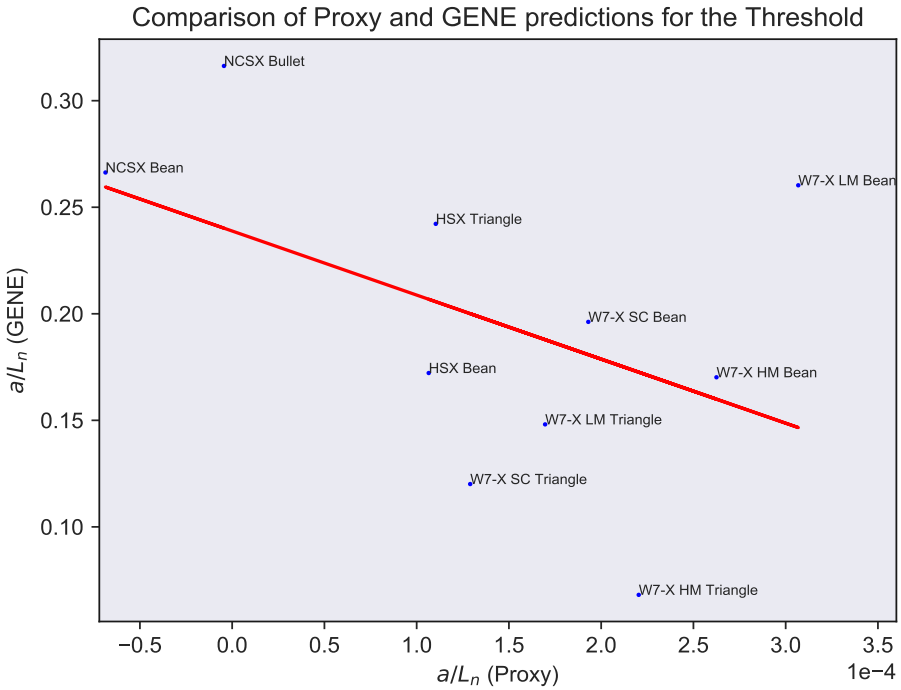


Figure 24: The graph displays a comparison between the threshold prediction from both the proxy, and GENE. The results from the proxy are on the x-axis, while the GENE results are on the y-axis. The red line indicates a linear fit on the data, a trend line.

| **Device/Configuration** | **Flux Tube** | **Simulation Threshold** | **Proxy Threshold** |
|---|---|---|---|
| DIII-D | Midplane | 0.3263 | $8.82\times10^{-3}$ |
| HSX | Bean | 0.1722 | $1.07\times10^{-4}$ |
| HSX | Triangle | 0.2422 | $1.11\times10^{-4}$ |
| W7-X HM | Bean | 0.1702 | $2.62\times10^{-4}$ |
| W7-X HM | Triangle | 0.0681 | $2.21\times10^{-4}$ |
| W7-X SC | Bean | 0.1962 | $1.93\times10^{-4}$ |
| W7-X SC | Triangle | 0.1201 | $1.29\times10^{-4}$ |
| W7-X LM | Bean | 0.2603 | $3.07\times10^{-4}$ |
| W7-X LM | Triangle | 0.1481 | $1.69\times10^{-4}$ |
| NCSX | Bean | 0.2663 | $-6.87\times10^{-5}$ |
| NCSX | Bullet | 0.3163 | $-4.44\times10^{-6}$ |

Table 2: The table provides an overview of the results of the proxy, compared to the thresholds as calculated by GENE.

# 6 Discussion

It is clear from figure (24) that the proxy produces a weak inverse correlation when compared with the GENE results. It is suspected that this is due to the ordering assumption that were made during the derivation of the proxy itself. In particular, when it was assumed that $\overline{\omega}_{da} << \omega$ in order to derive the identity equation (3.13). This assumption was found not to be true at marginal stability, as the magnetic drift frequency is not typically that small. It was made only for the purpose of being able to derive a workable form of the proxy. If a reasonable result is to be obtained, a correction to this derivation would have to avoid that ordering (chapter 7).

However, we also notice a smaller trend within the results (figure 25). Within a particular configuration of a stellarator, the proxy captures the differences accurately between the different flux tubes. Although only NCSX is displayed in figure (25), such a trend is visible for all stellarators, except for HSX. The proxy calculates the threshold at almost exactly the same value for HSX, between the bean and triangle flux tubes. This is not surprising as the magnetic field line structure, and the curvature are very similar between the bean and triangle flux tubes. This offers very little for the proxy to differentiate between the two flux tubes.

It is reasonable to think that the proxy predicts the correct threshold between flux tubes, as long as we restrict it to a particular magnetic configuration. However, the lack an of overall trend is still highly discouraging. Leading to the conclusion that the simplest version of the dispersion relation is not suitable for this purpose.

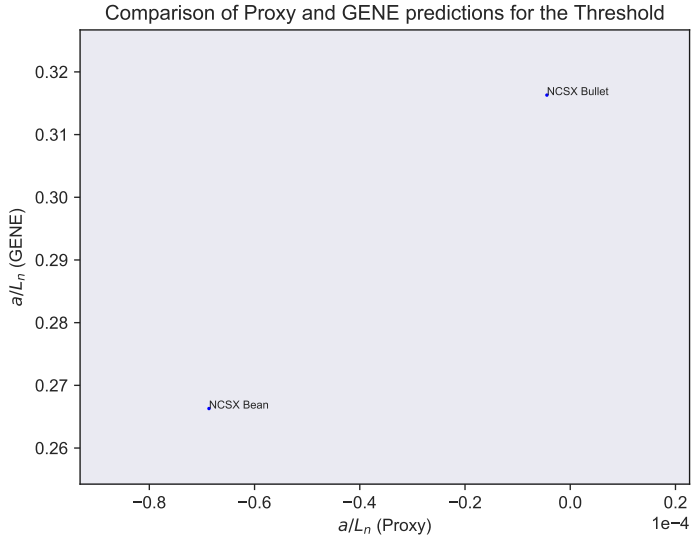


Figure 25: A cropped out section of figure (24).

We also notice that the proxy predicts the thresholds very close to zero, while GENE predicts them to be higher by 3 orders of magnitude for most cases. While the proxy is not expected to be highly accurate, this behaviour is very peculiar. Which leads to the conjecture that the proxy is possibly calculating $\tilde{\omega}_{de}$ as a very small quantity. This is possibly because we ordered the frequencies as such in the derivation.

It is important to also consider how a stellarator that has been optimised for the TEM threshold may behave. We know that tokamaks have higher thresholds but also a higher growth rate, while stellarators have a lower threshold but also a lower growth rate (figure 2). Therefore, the emphasis should also lie on ensuring that the optimised geometry does not inadvertently provide a magnetic geometry with lower thresholds, or with higher growth rates. However, the higher growth rates might not be a prohibitive factor, if the threshold is high enough from an operational standpoint. An ideal geometry, from the perspective of TEMs, would provide us with higher thresholds and a lower growth rates. Although, finding this point in the optimisation parameter space might be difficult, if at all possible.

# 7 An Alternative Approach

While the course followed in this work may have yielded a negative result, there are alternative ways to evaluate the integral as written in equation (3.11). The alternative method was suggested by Beer and Hammett (1996), where a dispersion relation was obtained using the distribution function given by

$$g = F_0 \frac{(\omega - \omega_*^T)}{(\omega - \omega_{dv})} J_0 \frac{e\phi}{T} \tag{7.1}$$

and substituting it in the quasi-neutrality condition to give us

$$-n_{0a}\frac{e_a\phi}{T_a} = -n_{0s}\frac{e_s\phi}{T_s}\int F_0 \frac{(\omega - \omega_*^T)}{(\omega - \omega_{dv})} d\mathbf{v} \tag{7.2}$$

where $F_0$ is a Maxwellian, the subscript 'a' refers to the adiabatic species, and 's' refers to the kinetic species (Shi et al., 2015; Biglari et al., 1989). And $\omega_*^T$ is given by

$$\omega_*^T = \omega_* \left[1 + \frac{L_n}{L_T}\left(\frac{v_\parallel^2}{2v_T^2} + \frac{\mu B}{v_T^2} - \frac{3}{2}\right)\right] \tag{7.3}$$

and

$$\omega_{dv} = \omega_d \frac{(v_\parallel^2 + \mu B)}{v_T^2} \tag{7.4}$$

and

$$\omega_d = \frac{k_y \rho_e v_T}{R} \tag{7.5}$$

By using closure approximations, equation (7.2) can be written as

$$-n_{0a}\frac{e_a\phi}{T_a} = -n_{0s}\frac{e_s\phi}{T_s}\left[R_0\left(\frac{\omega}{\omega_d}\right) + \frac{R}{L_n}R_1\left(\frac{\omega}{\omega_d}\right) + \frac{R}{L_T}R_2\left(\frac{\omega}{\omega_d}\right)\right] \tag{7.6}$$

where the factor of $R_0(y)$, $R_1(y)$, and $R_2(y)$ (while neglecting Finite Larmor Radius effects) are given by

$$R_0(y) = 1 - \frac{y}{2}Z^2\left(\sqrt{\frac{y}{2}}\right) \tag{7.7}$$

$$R_1(y) = \frac{1}{2}Z^2\left(\sqrt{\frac{y}{2}}\right) \tag{7.8}$$

$$R_2(y) = \left(\frac{y}{2} - \frac{1}{2}\right)Z^2\left(\sqrt{\frac{y}{2}}\right) + \frac{x}{2}Z\left(\sqrt{\frac{y}{2}}\right) \tag{7.9}$$

where $y = \omega/\omega_d$, and $Z(\zeta)$ is given by the plasma dispersion relation,

$$Z(\zeta) = \pi^{-1/2}\int_{-\infty}^{\infty}\frac{\exp\{-t^2\}}{t-\zeta}dt = 2i\exp\{-\zeta^2\}\int_{-\infty}^{i\zeta}\exp\{-t^2\}dt \tag{7.10}$$

We notice that the last term in equation (7.6) can be neglected as we have assumed a flat temperature profile, simplifying things considerably. This also helps speed up the computational component with fewer integrals to calculate. However, the original derivation is done from the perspective of the ITG instability. To do so, it ignores trapped particle effects, carried out at the toroidal limit ($k_\parallel = 0$), and the the distribution function used to carry out the work (without the adiabatic part), given by equation (7.1) is more suited to ions, as found by Proll (2014).

However, the methodology can of course be adapted towards solving the research questions posed in this project. This can be achieved by starting with the appropriate distribution function as given by

$$g_a = \frac{e_a}{T_a}\overline{J_0\phi}\frac{(\omega - \omega_{*a}^T)}{(\omega - \bar{\omega}_{da})}f_{a0} \tag{7.11}$$

as described in chapter 3. From here, we may go forward with similar steps to what is described in this work until the crux of the issue as presented in equation (3.11). At this point, one ought to carry out a treatment similar to the one presented by Beer and Hammett (1996), which puts equation (7.6) in the form

$$-n_{0a}\frac{e_a\phi}{T_a} = -n_{0s}\frac{e_s\phi}{T_s}\left[R_0\left(\frac{\omega}{\overline{\omega}_d}\right) + \frac{R}{L_n}R_1\left(\frac{\omega}{\overline{\omega}_d}\right) + \frac{R}{L_T}R_2\left(\frac{\omega}{\overline{\omega}_d}\right)\right] \tag{7.12}$$

where the $R_0$, $R_1$, and $R_2$ factors take the form given by figures (26)a, (26)b, and (26)c. Which is an exact match to the result shown in Beer and Hammett (1996). Of course this is not surprising, as the magnitude and shape of the factors should not change between the two relations.

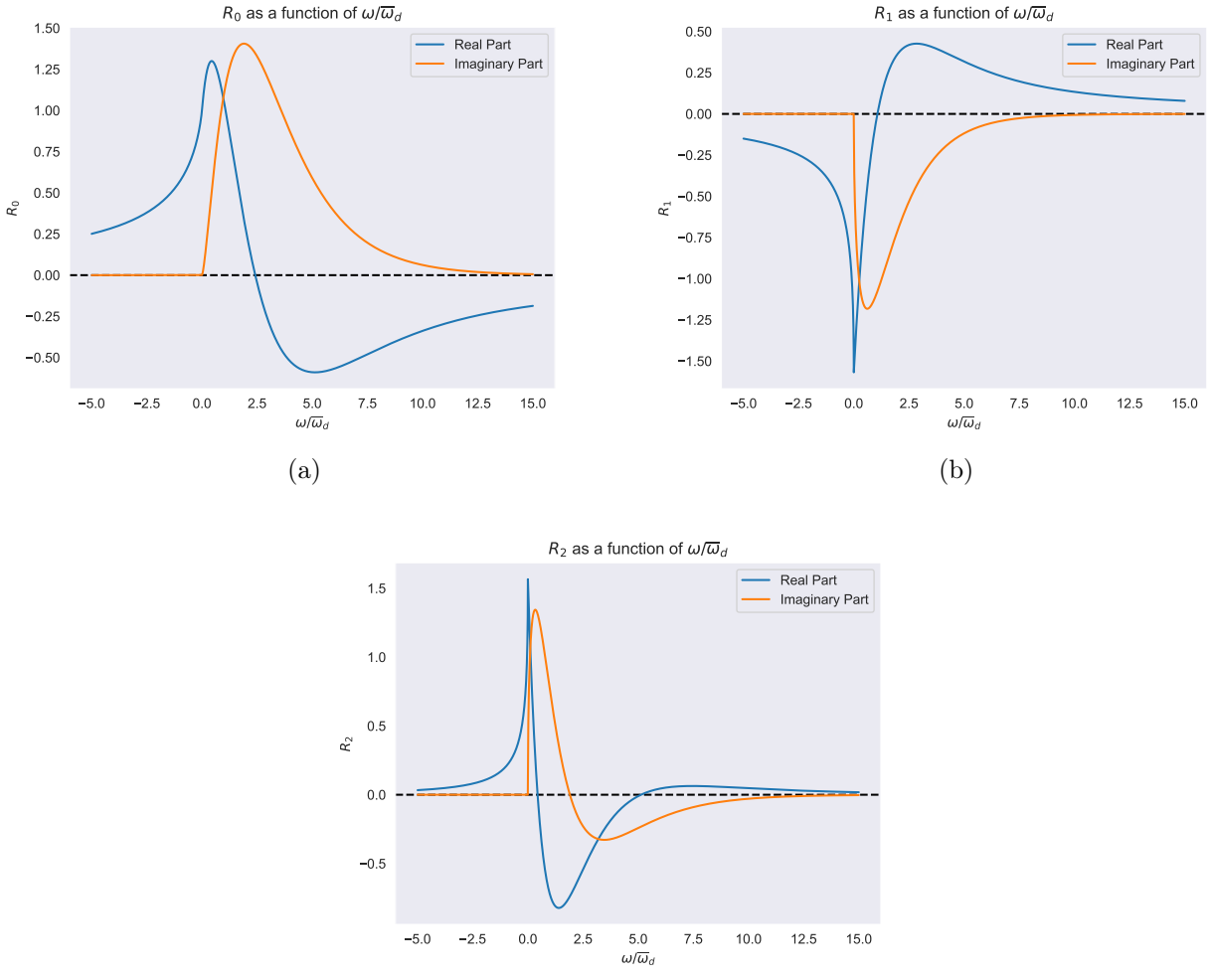


(a) (b)

(c)

Figure 26: The three figures show the shape and magnitude of equations (7.7), (7.8), and (7.9). They cross-validates Beer and Hammett (1996) before carrying on to perform further work.

We can now calculate the dispersion relation which is given by,

$$0 = D(\omega) = R_0\left(\frac{\omega}{\overline{\omega}_d}\right) + \frac{R}{L_n}R_1\left(\frac{\omega}{\overline{\omega}_d}\right) + \frac{R}{L_T}R_2\left(\frac{\omega}{\overline{\omega}_d}\right) + \frac{T_s}{T_a} \tag{7.13}$$

where it is assumed that $n_{0a} = n_{0s}$, and that $q_a = q_s$.

Equation (7.13) can be further simplified when considering a flat temperature profile ($1/L_T = 0$), as in all of the simulations that this work is comparing with. In order to find the critical gradient, we will also re-write the equation in terms of $R/L_n$, giving us,

$$\frac{R}{L_n} = y - \frac{4}{Z^2(\sqrt{\frac{y}{2}})} \tag{7.14}$$

which is calculated using equations (7.7) and (7.8), and $y = \omega/\overline{\omega}_d$. Using this relation, we may now have a look at what the function looks like (figure 27), such that we may know what to do next. Figure (27) show the real and imaginary parts of equation (7.14), however, we are interested in the imaginary part of the result as this is the part that gives us the growth rate.

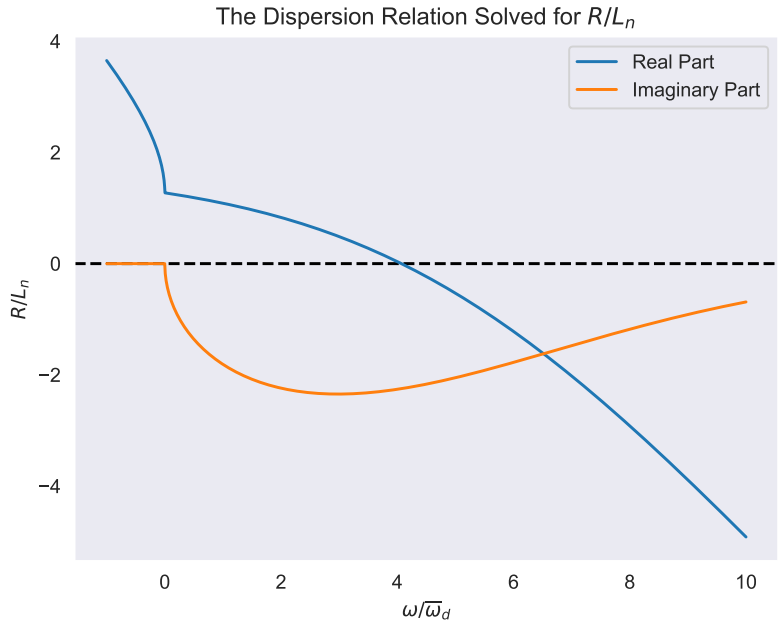


Figure 27: The image displays the real and imaginary parts of equation (7.14).

As is clear from figure (27), there is a minima in the imaginary part which relates to a specific $R/L_n$. However, to be able to integrate this into an optimisation algorithm, we need to eliminate mode frequency dependency from the relation as we would not have prior information about the mode frequency in a particular device/geometry during the optimisation process.

We may achieve this by using variational principle analysis (Gelfand et al., 2000; Russak, 2002) to obtain an approximation for the mode structure. This could then be used to circumvent the need to know the mode frequency in advance, whilst performing the optimisation process. The process has been used previously in Helander et al. (2013) and Proll (2014). However, this has not been calculated here, as it is outside the scope of this thesis.

# 8 Conclusion

Considering the harsh deadline imposed on humanity by global warming, and the ever-growing need for energy, we require a continuous source of energy that is also energy dense. Nuclear fusion is something that satisfies all of the requirements that we have, except for one, which is that it does not yet exist at a commercial scale. To achieve this goal, our ability to predict and control turbulence is crucial, as it sets the energy confinement time in a magnetically confined fusion reactor. Although there are multiple ways to achieve fusion, we focused on the stellarator type design, and on optimising it to a higher critical gradient in the TEM. We aimed to achieve this by deriving a dispersion relation that describes TEMs, and to then use it to obtain a simplified expression for the critical gradient.

Whilst we were successful in obtaining such a relation, the results indicated a weak inverse correlation with the simulation results by GENE. This is most likely the result of using the wrong frequency ordering choices when attempting to solve a crucial integral. The proxy also tends to estimate thresholds close to zero, which is not the case in reality. This is also most likely due to the ordering assumptions made in the derivation of the proxy.

An alternative way of obtaining a proxy has been suggested, but ridding the final relation of the mode frequency dependency is key. We can achieve this by using the variational principle to obtain an approximate mode structure. This structure can then be used in the optimisation process. Although this approach will not rid the relation of the mode frequency, it will provide us with an approximation that enables us to proceed with the optimisation process.

It is important that we preserve the quasi-symmetry or other unique properties (like quasi-isodynamicity in W7-X) of the devices we aim to optimise, as the loss of these properties might lead to higher levels of NC transport, which is not desirable. Proll et al. (2015) details how the NC effective ripple went up by an order of magnitude due to the loss of quasi-symmetry in HSX. But Mynick et al. (2011) have found configurations for NCSX where both turbulent, and NC transport levels were reduced. Although the simulations were carried out over the ITG instability, there is reason to believe that this will help TEM instabilities too, due to the improved average curvature. In fact, any channel that benefits from an improved average curvature stands to be stabilised. This was confirmed with the ETG mode simulations that were carried out (Mynick et al., 2011). They have also found that the improved average curvature is achieved by deformations which displace inner flux surfaces outward more than the outer ones, similar to the effect of raising the plasma $\beta$, which also has an affect in reducing turbulence levels.

From the perspective of this particular thesis, an optimised geometry would provide us with higher thresholds and a lower growth rates for the TEM. The next logical step would then be to incorporate the ITG and ETG channels in the optimisation process. The ultimate goal however, is a holistically optimised stellarator, which can reduce heat flux but retain particle flux to flush out impurities.

## Acknowledgements

The author primarily thanks Dr. J.H.E. Proll and Dr. H.E. Mynick for their supervision through this project, and allowing the opportunity to work on an exciting topic. The discussions that were had with Dr. G.W. Hammett, Mr. A. Perek, Mr. A. Ho, Mr. C.M. Moreno, and Mr. R. Mackenbach were also invaluable towards the project. In addition to which, the author would like to thank the Max-Planck-Institut für Plasmaphysik (Greifswald), and the Princeton Plasma Physics Laboratory for hosting the project.

This work was carried out at the Max-Planck-Institut für Plasmaphysik (Greifswald), the Princeton Plasma Physics Laboratory, and the Technische Universiteit Eindhoven between June 2018 and February 2019, with support from Fusenet (fusenet.eu).

## References

A. F. Almagri, D. T. Anderson, F. S. B. Anderson, P. H. Probert, J. L. Shohet, and J. N. Talmadge. A helically symmetric stellarator (hsx). *IEEE Transactions on Plasma Science*, 27(1):114–115, 1999.

M. Barnes. Trinity: A unified treatment of turbulence, transport, and heating in magnetized plasmas. *arXiv preprint arXiv:0901.2868*, 2009.

M. A. Beer and G. W. Hammett. Toroidal gyrofluid equations for simulations of tokamak turbulence. *Physics of Plasmas*, 3(11):4046–4064, 1996.

H. Biglari, P. Diamond, and M. Rosenbluth. Toroidal ion-pressure-gradient-driven drift instabilities and transport revisited. *Physics of Fluids B: Plasma Physics*, 1(1):109–118, 1989.

H. Biglari, P. Diamond, and P. Terry. Influence of sheared poloidal rotation on edge turbulence. *Physics of Fluids B: Plasma Physics*, 2(1):1–4, 1990.

A. H. Boozer. Physics of magnetically confined plasmas. *Reviews of modern physics*, 76(4):1071, 2005.

P. J. Catto. Linearized gyro-kinetics. *Plasma Physics*, 20(7):719, 1978.

B. I. Cohen, J. Krommes, W. Tang, and M. Rosenbluth. Non-linear saturation of the dissipative trapped-ion mode by mode coupling. *Nuclear fusion*, 16(6):971, 1976.

W. A. Cooper. Ballooning instabilities in tokamaks with sheared toroidal flows. *Plasma physics and controlled fusion*, 30(13):1805, 1988.

W. A. Cooper, D. Singleton, and R. Dewar. Spectrum of ballooning instabilities in a stellarator. *Physics of Plasmas*, 3(1):275–280, 1996.

S. Cowley. Gyro-kinetics lectures. from iter time-scales to gyro-kinetics. *ox.ac.uk*, 2018.

A. M. Dimits, G. Bateman, M. Beer, B. Cohen, W. Dorland, G. Hammett, C. Kim, J. Kinsey, M. Kotschenreuther, A. Kritz, et al. Comparisons and physics basis of tokamak transport models and turbulence simulations. *Physics of Plasmas*, 7(3):969–983, 2000.

D. Ernst, N. Basse, W. Dorland, C. Fiore, L. Lin, A. Long, M. Porkolab, K. Zeller, and K. Zhurovich. Identification of tem turbulence through direct comparison of nonlinear gyrokinetic simulations with phase contrast imaging density fluctuation measurements. 2009.

X. Garbet, P. Mantica, C. Angioni, E. Asp, Y. Baranov, C. Bourdelle, R. Budny, F. Crisanti, G. Cordey, L. Garzotti, et al. Physics of transport in tokamaks. *Plasma Physics and Controlled Fusion*, 46(12B):B557, 2004.

X. Garbet, Y. Idomura, L. Villard, and T. Watanabe. Gyrokinetic simulations of turbulent transport. *Nuclear Fusion*, 50(4):043002, 2010.

I. M. Gelfand, R. A. Silverman, et al. *Calculus of variations*. Courier Corporation, 2000.

General Atomics. Diii-d, 2018. URL `http://www.ga.com/diii-d`.

T. Hahm and K. Burrell. Flow shear induced fluctuation suppression in finite aspect ratio shaped tokamak plasma. *Physics of Plasmas*, 2(5):1648–1651, 1995.

P. Helander and D. J. Sigmar. *Collisional transport in magnetized plasmas*, volume 4. Cambridge University Press, 2005.

P. Helander, J. H. E. Proll, and G. G. Plunk. Collisionless microinstabilities in stellarators. i. analytical theory of trapped-particle modes. *Physics of Plasmas*, 20(12):122505, 2013.

M. Hirsch, J. Baldzuhn, C. Beidler, R. Brakel, R. Burhenn, A. Dinklage, H. Ehmler, M. Endler, V. Erckmann, Y. Feng, et al. Major results from the stellarator wendelstein 7-as. *Plasma Physics and Controlled Fusion*, 50(5):053001, 2008.

W. Horton. Drift waves and transport. *Reviews of Modern Physics*, 71(3):735, 1999.

F. Jenko. Massively parallel vlasov simulation of electromagnetic drift-wave turbulence. *Computer physics communications*, 125(1-3):196–209, 2000.

F. Jenko, W. Dorland, M. Kotschenreuther, and B. Rogers. Electron temperature gradient driven turbulence. *Physics of Plasmas*, 7(5):1904–1910, 2000.

R. E. LaQuey, S. Mahajan, P. Rutherford, and W. Tang. Nonlinear saturation of the trapped-ion mode. *Physical Review Letters*, 34(7):391, 1975.

J. D. Lawson. Some criteria for a power producing thermonuclear reactor. *Proceedings of the Physical Society. Section B*, 70(1):6, 1957.

B. E. Layton. A comparison of energy densities of prevalent energy sources in units of joules per cubic meter. *International Journal of Green Energy*, 5(6):438–455, 2008.

Z. Lin, T. S. Hahm, W. Lee, W. M. Tang, and R. B. White. Turbulent transport reduction by zonal flows: Massively parallel simulations. *Science*, 281(5384):1835–1837, 1998.

J. L. Luxon. A design retrospective of the diii-d tokamak. *Nuclear Fusion*, 42(5):614, 2002.

F. Merz. *Gyrokinetic simulation of multimode plasma turbulence*. PhD thesis, Universität Münster, 2008.

H. Mynick. Transport optimization in stellarators. *Physics of plasmas*, 13(5):058102, 2006.

H. Mynick, N. Pomphrey, and P. Xanthopoulos. Reducing turbulent transport in toroidal configurations via shaping. *Physics of Plasmas*, 18(5):056101, 2011.

J. Nührenberg, W. Lotz, P. Merkel, C. Nührenberg, U. Schwenn, E. Strumberger, and T. Hayashi. Overview on wendelstein 7-x theory. *Fusion Technology*, 27(3T):71–78, 1995.

J. Proll, H. Mynick, P. Xanthopoulos, S. Lazerson, and B. Faber. Tem turbulence optimisation in stellarators. *Plasma Physics and Controlled Fusion*, 58(1):014006, 2015.

J. H. E. Proll. Trapped-particle instabilities in quasi-isodynamic stellarators, 2014.

J. H. E. Proll, P. Helander, J. W. Connor, and G. Plunk. Resilience of quasi-isodynamic stellarators against trapped-particle instabilities. *Physical review letters*, 108(24):245002, 2012.

A. Reiman, G. Fu, S. Hirshman, L. Ku, D. Monticello, H. Mynick, M. Redi, D. Spong, M. Zarnstorff, B. Blackwell, et al. Physics design of a high-quasi-axisymmetric stellarator. *Plasma Physics and Controlled Fusion*, 41(12B):B273, 1999.

F. Romanelli, P. Barabaschi, P. Borba, G. Federici, L. Horton, R. Neu, D. Stork, and H. Zohm. A roadmap to the realization of fusion energy. In *Proc. IEEE 25th Symp. Fusion Eng*, pages 1–4, 2013.

M. Romanelli, G. Regnoli, and C. Bourdelle. Numerical study of linear dissipative drift electrostatic modes in tokamaks. *Physics of Plasmas*, 14(8):082305, 2007.

I. Russak. *Calculus of variations MA 4311 lecture notes*. Monterey, California: Naval Postgraduate School., 2002.

E. Shi, A. Hakim, G. Hammett, I. Abel, and T. Stoltzfus-Dueck. Recent results from the gkeyll discontinuous galerkin kinetic code, 2015.

A. Subbotin, M. Mikhailov, V. Shafranov, M. Y. Isaev, C. Nührenberg, J. Nührenberg, R. Zille, V. Nemov, S. Kasilov, V. Kalyuzhnyj, et al. Integrated physics optimization of a quasi-isodynamic stellarator with poloidally closed contours of the magnetic field strength. *Nuclear fusion*, 46(11): 921, 2006.

W. M. Tang. Microinstability theory in tokamaks. *Nuclear Fusion*, 18(8):1089, 1978.

P. Terry. Suppression of turbulence and transport by sheared flow. *Reviews of Modern Physics*, 72 (1):109, 2000.

The Economist. Stellar work, 2015. Accessed on: 07/12/18.

F. Warmer, P. Xanthopoulos, J. Proll, C. Beidler, Y. Turkin, and R. Wolf. First steps towards modeling of ion-driven turbulence in wendelstein 7-x. *Nuclear Fusion*, 58(1):016017, 2017.

J. Wesson and D. J. Campbell. *Tokamaks*, volume 149. Oxford university press, 2011.

P. Xanthopoulos, W. A. Cooper, F. Jenko, Y. Turkin, A. Runov, and J. Geiger. A geometry interface for gyrokinetic microturbulence investigations in toroidal configurations. *Physics of Plasmas*, 16(8): 082303, 2009.

M. Zarnstorff, L. Berry, A. Brooks, E. Fredrickson, G. Fu, S. Hirshman, S. Hudson, L. Ku, E. Lazarus, D. Mikkelsen, et al. Physics of the compact advanced stellarator ncsx. *Plasma Physics and Controlled Fusion*, 43(12A):A237, 2001.

# A The Numerical Calculation of the Proxy

```
#!/usr/bin/env python3
# -*- coding: utf-8 -*-

"""
This file is written in order to predict a critical gradient
from an example magnetic geometry, such that it can be
compared to simulation data.

This specific script only produces the values of
the integrals. It cycles through all the geometries
that have been chosen, and calculates the desired
integrals in a loop.

This script has not been parallelised.
"""

import numpy as np
import scipy.interpolate as interp
from datetime import datetime


#All of the available GIST output files
geo = ['gist_ncsx_vac_2_s05.dat',
       'gist_ncsx_vac_s05.dat',
       'gist_d3d_s05.dat',
       'gist_hsx_vac_s05_bean.dat',
       'gist_hsx_vac_s05_triangle.dat',
       'gist_w7xsc1_vac_s05_bean.dat',
       'gist_w7xsc1_vac_s05_triangle.dat',
       'gist_w7x_vac_s05.dat',
       'gist_w7x_vac_2_s05.dat',
       'gist_w7xlm1_vac_s05_bean.dat',
       'gist_w7xlm1_vac_s05_triangle.dat']

startTime = datetime.now()

#############

#The pressure gradient data, taken from the GIST files mentioned above
mydpdx = {geo[0][:-4] : 0.0003669,
          geo[1][:-4] : 0.0003669,
          geo[2][:-4] : -0.0087216,
          geo[3][:-4] : 0.0000000,
          geo[4][:-4] : 0.0000000,
          geo[5][:-4] : -0.0000696,
          geo[6][:-4] : -0.0000696,
          geo[7][:-4] : 0.0000000,
          geo[8][:-4] : 0.0000000,
          geo[9][:-4] : -0.0000399,
          geo[10][:-4] : -0.0000399}

#Defining the number of samples to be integrated over, for the composite
#trapezoidal rule.
samples = 1e5
samples_2 = 1e5
#############

"""
functions
"""

#Heaviside function
def well(lamb):
    return np.heaviside((0.999/lamb)-B,B)
```

```
65
66 #Bounce time integral
67 def tau(x):
68     m = well(x) / np.sqrt(1-(x*B))
69     m[np.isnan(m)] = 0
70     return m
71
72 #Integral 2
73 def omb(x):
74     m = (well(x)*kap*(1-((x*B)/2))) / (1-(x*B))
75     m[np.isnan(m)] = 0
76     return m
77
78 #Integral 3
79 def lambda_int(x,y):
80     st_int = np.divide(x,y)
81     st_int[np.isnan(st_int)] = 0
82     integral = np.trapz(st_int,x=lamb_samples,axis=-1) / len(Blist)
83     return integral
84
85 """
86 Loop
87 """
88
89 n=0
90 while n in range(0,len(geo)):
91
92     mini_timer = datetime.now()
93
94     data = np.loadtxt('../geometries/'+geo[n], skiprows=10)
95
96     #Discreet B, to be interpolated
97     Blist = data[:,3]
98     b0 = 0.5*(max(Blist)+min(Blist))
99     bamp = 0.5*(max(Blist)-min(Blist))
100
101    #Samples present currently
102    nz = np.linspace(0,len(Blist),len(Blist))
103    #Samples for Interpolation
104    nz1 = np.linspace(0,len(Blist),samples)
105
106    #Interpolation
107    B = interp.splrep(nz,Blist,s=0)
108    B = interp.splev(nz1, B, der=0)
109
110    #Interpolation
111    klist = data[:,5] - (0.5*(mydpdx[geo[n][:-4]]/data[:,3]))
112    kap = interp.splev(nz1,interp.splrep(nz,klist,s=0),der=0)
113
114    #Creating samples for lamda
115    lamb_samples = np.arange(1/(max(Blist))-(0.0000001*max(Blist)),
116                1/min(Blist),(1/min(Blist)-1/max(Blist))/(samples_2-1))
117
118    tau_val = []
119
120    #Integrating bounce time integral
121    for lamb in lamb_samples:
122        I = np.trapz(tau(lamb),x=nz1,axis=-1) / len(Blist)
123        tau_val.append(I)
124
125    omb_val = []
126
127    #Integrating integral 2
128    for lamb in lamb_samples:
129        I1 = np.trapz(omb(lamb),x=nz1,axis=-1) / len(Blist)
130        omb_val.append(I1)
```

```
131
132     st_int = np.divide(omb_val,tau_val)
133     st_int[np.isnan(st_int)] = 0
134
135     #Integrating integral 3
136     integral = np.trapz(st_int,x=lamb_samples,axis=-1) / len(Blist)
137
138     print('The integral value for '+ geo[n][:-4] +' is: ',
139           lambda_int(omb_val,tau_val))
140
141     n += 1
142
143     print('Time taken for this run: ',datetime.now() - mini_timer)
144
145
146
147 print('Time taken overall: ',datetime.now() - startTime)
```

# B Discrepancies in the Numerical Solutions

In the process of analysing scripts for the calculation of the proxy, numerical discrepancies were discovered between different coding languages. In this case, between mathematica and python.

To highlight this better, we will first solve a problem with a heaviside step function, for which we already know an analytical solution.

$$f(x) = \int_1^4 H[x-2]x^3 dx = 60 \tag{B.1}$$

We can now compare this to the results we obtain from both mathematica and python. When the trapezoidal rule is used in both cases, mathematica provides us with a result of 59.99. However, python provides a much more accurate answer of 60. Although there are floating point errors in the answer calculated by python (at the fifth decimal point), it is considerably more accurate when compared to the value calculated by mathematica.

It is important to note that the black box nature of mathematica prevents further investigation into this issue. However, it does seem as though the two languages approach the heaviside function from a fundamentally different approach. Mathematica tends to consistently underestimate the value, while python tends to overestimate the value ever so slightly. This is reflected in the data, when further decimal points are displayed.

Although this would not change the results of the thesis, it would considerably change the magnitude of the thresholds that have been obtained from the proxy. Therefore, it is something to be aware of when trying to replicate this work.